Check for updates

Evolution of delayed resistance to immunotherapy in a melanoma responder

David Liu[1,2,23], Jia-Ren Lin [3,23], Emily J. Robitschek[1,2], Gyulnara G. Kasumova[4], Alex Heyde[5,6], Alvin Shi[2,7], Adam Kraya[8], Gao Zhang[9,10], Tabea Moll[11], Dennie T. Frederick[11], Yu-An Chen [3], Shu Wang[3], Denis Schapiro [3,12], Li-Lun Ho[2,7], Kevin Bi[1,2], Avinash Sahu[1], Shaolin Mei[1,3], Benchun Miao[11], Tatyana Sharova[4], Christopher Alvarez-Breckenridge[13], Jackson H. Stocking [11], Tommy Kim[4], Riley Fadden[11], Donald Lawrence[11], Mai P. Hoang [14], Daniel P. Cahill[13], Mohsen Malehmir [2,4], Martin A. Nowak [5,6,15], Priscilla K. Brastianos [11], Christine G. Lian[16], Eytan Ruppin [17], Benjamin Izar [18,19], Meenhard Herlyn[9], Eliezer M. Van Allen [1,2], Katherine Nathanson [8,20,21], Keith T. Flaherty[11], Ryan J. Sullivan [11], Manolis Kellis [2,7], Peter K. Sorger [3,22] and Genevieve M. Boland [2,4 ✉]

Despite initial responses[1-3], most melanoma patients develop resistance[4] to immune checkpoint blockade (ICB). To understand the evolution of resistance, we studied 37 tumor samples over 9 years from a patient with metastatic melanoma with complete clinical response to ICB followed by delayed recurrence and death. Phylogenetic analysis revealed co-evolution of seven lineages with multiple convergent, but independent resistance-associated alterations. All recurrent tumors emerged from a lineage characterized by loss of chromosome 15q, with post-treatment clones acquiring additional genomic driver events. Deconvolution of bulk RNA sequencing and highly multiplexed immunofluorescence (t-CyCIF) revealed differences in immune composition among different lineages. Imaging revealed a vasculogenic mimicry phenotype in NGFR^{hi} tumor cells with high PD-L1 expression in close proximity to immune cells. Rapid autopsy demonstrated two distinct NGFR spatial patterns with high polarity and proximity to immune cells in subcutaneous tumors versus a diffuse spatial pattern in lung tumors, suggesting different roles of this neural-crest-like program in different tumor microenvironments. Broadly, this study establishes a high-resolution map of the evolutionary dynamics of resistance to ICB, characterizes a de-differentiated neural-crest tumor population in

melanoma immunotherapy resistance and describes site-specific differences in tumor–immune interactions via longitudinal analysis of a patient with melanoma with an unusual clinical course.

ICB has revolutionized cancer therapy across multiple solid tumor types. While 40–45% of patients with metastatic melanoma respond to PD-1 blockade[1-3], the majority succumb due to primary, adaptive or acquired resistance[4]. A diverse set of resistance mechanisms have been identified including β-catenin activation[5], *PTEN* loss[6-8], loss of antigen-presentation machinery[9,10], impaired interferon-γ responsiveness[9,11], genome instability and aneuploidy[12,13], cell-cycle dysregulation[14] and phenotype selection[15-17]. How these mechanisms emerge, interact and contribute to resistance within patients remains poorly understood. Longitudinal tumor samples enable study of the time course of response, shedding light on tumor heterogeneity[18], tumor evolution and acquired resistance. Previous studies have demonstrated intratumoral heterogeneity in many solid tumor types, including melanoma[19-23] and some studies have sequenced tumors longitudinally to examine evolution of resistance to chemotherapy[24,25], targeted therapy[26] and immunotherapy[10,13]. We generated a unique dataset of 37 longitudinally collected tumors to investigate the evolution of ICB resistance from a responder to ICB with eventual recurrence and death

from disease across 9 years, including the primary tumor, metastatic recurrence, pre-treatment, on-treatment, post-progression and rapid autopsy time points. While previous efforts have focused on sequential tumor analysis in ICB[27,28] with limited modalities (for example immune markers and microenvironment) or span a limited clinical timeframe, our study represents a large and in-depth study of tumor and microenvironmental evolution of an individual across all phases of his melanoma treatment from diagnosis to rapid autopsy. We performed whole-exome sequencing (WES), RNA sequencing (RNA-seq) and highly multiplexed protein immunofluorescence (t-CyCIF; Methods, Fig. 1 and Supplementary Table 1). The patient's clinical course is detailed in Fig. 1a.

Phylogenetic analysis integrating single-nucleotide variants and copy-number alterations (Methods) demonstrated a common tumor ancestor with a mutational spectrum consistent with UV damage, 618 shared mutations, driver hotspot mutations in *IDH1* (p.R132C) and *MAP2K1* (MEK1; p.E203K) and mutations in cancer driver genes *CTNNB1* (β-catenin; p.R582W) and *ARID2* (p.P1664S) (Extended Data Figs. 1 and 2). No driver mutations in *BRAF*, *NF1* or *NRAS/HRAS/KRAS* were detected. All tumors shared loss of heterozygosity (LOH) in segments of chromosome 3q, 6q, 9, 10 and 20 (Extended Data Fig. 3), which spanned tumor suppressors (*CDKN2A/B*; *PTEN*), interferon-γ pathway genes (*IFNGR1*; *JAK2*) and the chromatin remodeler gene *ARID1B*. Analysis revealed the coexistence and evolution of seven lineages at therapy onset, each having distinct genomic features (Fig. 1a,b, Extended Data Figs. 3–5 and Supplementary Fig. 1), including whole-genome doubling, loss of allelic chromosomal segments and gains of mutational clusters, with the most recent common ancestor being the primary tumor. Lineage 0 ($n=1$) was characterized by a genome doubling of the original primary clone in a recurrent lesion observed nearly 4 years later. All other lineages descended from a nongenome-doubled subclone with ten additional mutations. Lineage 1 ($n=8$ tumors) exhibited substantial spatial and temporal heterogeneity with the most recent common ancestor (MRCA) the common ancestor of lineages 1–6 without additional distinguishing copy-number alterations or mutations. Lineage 2 ($n=4$) included one pre-treatment tumor and was characterized by an early LOH of part of chromosome 2q, followed by a genome doubling event in three of four tumors in the lineage. Lineage 3 ($n=16$) included bowel and brain early recurrences and all subsequent treatment-resistant lesions and was characterized by an allelic chromosome 15q deletion. Lineage 4 ($n=3$) was limited to the head and neck and shared a cluster of nine distinct acquired mutations. Lineage 5 ($n=2$) was found at one time point (day (D)29) colocated spatially and was characterized by partial allelic loss of chromosome 19q. Lineage 6 ($n=2$) spanned two skin lesions (chin, D27; left groin, D92) with six distinct acquired mutations. The relationships between the MRCA of each lineage are shown in Fig. 1b and highlight the diversity and continued evolution of melanoma within a single patient.

Across all lineages, we observed multiple genomic resistance-associated alterations. Nearly all tumors (33 of 37) had a homozygous deletion in PTEN (Supplementary Table 1) arising from a common LOH of chromosome 10 with a focal deletion of a ~500-kB region overlapping *PTEN*. In 19 tumors, PTEN was examined via immunohistochemistry (IHC) and all were negative, including two tumors without a *PTEN* homozygous deletion (Supplementary Fig. 2), suggesting multiple routes to a PTEN-null phenotype. Post-treatment-resistant lesions arose out of lineage 3, distinguished by regional loss of 15q, including *B2M* required for major histocompatibility complex (MHC)-I antigen presentation[10]. Notably, we found four independent whole-genome duplication events: (1) in the common ancestor of three tumors (T4, T9, T10) in lineage 2 before ICB; (2) twice in lineage 3 (small bowel metastasis and brain metastasis independently) distinguishing the post-treatment-resistant tumors from earlier tumors in the lineage;

and (3) in lineage 0 before ICB. Tumors with genome doubling had evidence of increased chromosomal instability with higher aneuploidy[29], which has been associated with immunotherapy resistance[12] (Mann–Whitney *U*-test, $P < 0.001$; Extended Data Fig. 6).

'Early' resistant lesions (small bowel, R1, D1028 and brain metastasis, R2, D1,169) showed accumulation of multiple genomic alterations associated with immunotherapy resistance: *PTEN* loss, 15q deletion (including *B2M*) and genome doubling, as well as additional driver alterations (for example *CDKN2A* homozygous deletion). 'Late' resistant tumors (R3.1, R3.2 and autopsy tumors) descended from the small bowel (R1, D1,028) clone with *CDKN2A* homozygous deletion and demonstrated additional LOH of Chr11, including a frequently deleted region in melanoma[30], including DNA damage sensor and response genes *ATM* and *CHEK1* and epigenetic regulator *KMT2A* (Fig. 1c and Supplementary Fig. 3).

Tumors evolve in parallel with their tumor microenvironment (TME) and tumor mutational status provides only a partial picture. Therefore, we characterized the TME using deconvolution of bulk RNA-seq using single-cell-derived signatures of immune cell subsets[17] and analysis of cyclic multiplexed immunofluorescence (t-CyCIF) (Methods). Relative to a large cohort of aPD-1-treated patients with melanoma[31], these tumors had a low overall immune score (Extended Data Fig. 7), consistent with t-CyCIF imaging, demonstrating that most tumors were immunologically 'cold' with low levels of immune cells in the TME (Fig. 2a). Immune scores derived from RNA-seq and corresponding immune cell proportions inferred using t-CyCIF correlated well (Supplementary Fig. 4). We next examined the association of lineage with specific immune cell subsets. Despite relatively few samples for each lineage, we detected a statistically significant overall association of lineage with expression of a CD4+ T cell and regulatory T cell signatures (analysis of variance (ANOVA), $P = 0.018$, Benjamini–Hochberg false discovery rate $q = 0.09$ (adjusted for ten immune signatures), both, Fig. 2b). Comparing tumors in the resistant lineage (lineage 3) versus other lineages, we observed a trend of lower CD4+ and CD8+ T cell signature scores (Fig. 2c) with the notable exception of CD4+ regulatory T cells being higher in lineage 3, consistent with the hypothesis of a more immunosuppressive environment in the resistant lineage. However, with data from only three tumors in lineage 3, these observations were mostly not statistically significant. Examining changes in the TME over time (Fig. 2d), we observed higher levels of CD8+ effector T cells and CD4+ Foxp3 helper T cells in the immediate post-IO initiation period (D27–62) compared to the later IO period (D76–109), particularly in the tumor border regions (Fig. 2e, Extended Data Figs. 7b–d and 8).

We also performed a Hallmark cancer gene set analysis, using single sample gene set enrichment analysis (GSEA)[32] of Hallmark cancer gene sets[33] (Methods) to characterize activity levels in samples and association with lineage and time. No individual gene sets were statistically significantly associated with lineage or time after multiple hypothesis correction (Supplementary Fig. 5a–c), but principal-component analysis (PCA) dimensionality reduction suggested clustering of lineage 2 tumors driven in part by increased immune activity (Supplementary Fig. 5d,e).

We then examined the relative spatial orientation and arrangement of tumor and immune cell subsets across tumors using t-CyCIF (Supplementary Table 1; https://www.cycif.org/data/liu-lin-2019/). We observed vascular-pattern networks consisting of nonendothelial lined neural-crest-like (NGFR^hi) tumor cells consistent with vascular mimicry (Fig. 3a and Supplementary Fig. 6)[34], a pattern previously associated with an aggressive and therapy resistant phenotype[15,16,35]. Clustering of single-cell t-CyCIF data (Fig. 3b and Methods) showed a distinct PD-L1^hiNGFR^hi tumor cell cluster (Fig. 3c and Extended Data Fig. 9a) and spatial enrichment analysis (Methods) showed cluster enrichment in proximity to immune cells (Fig. 3d). At the time of late recurrence, the patient was enrolled on
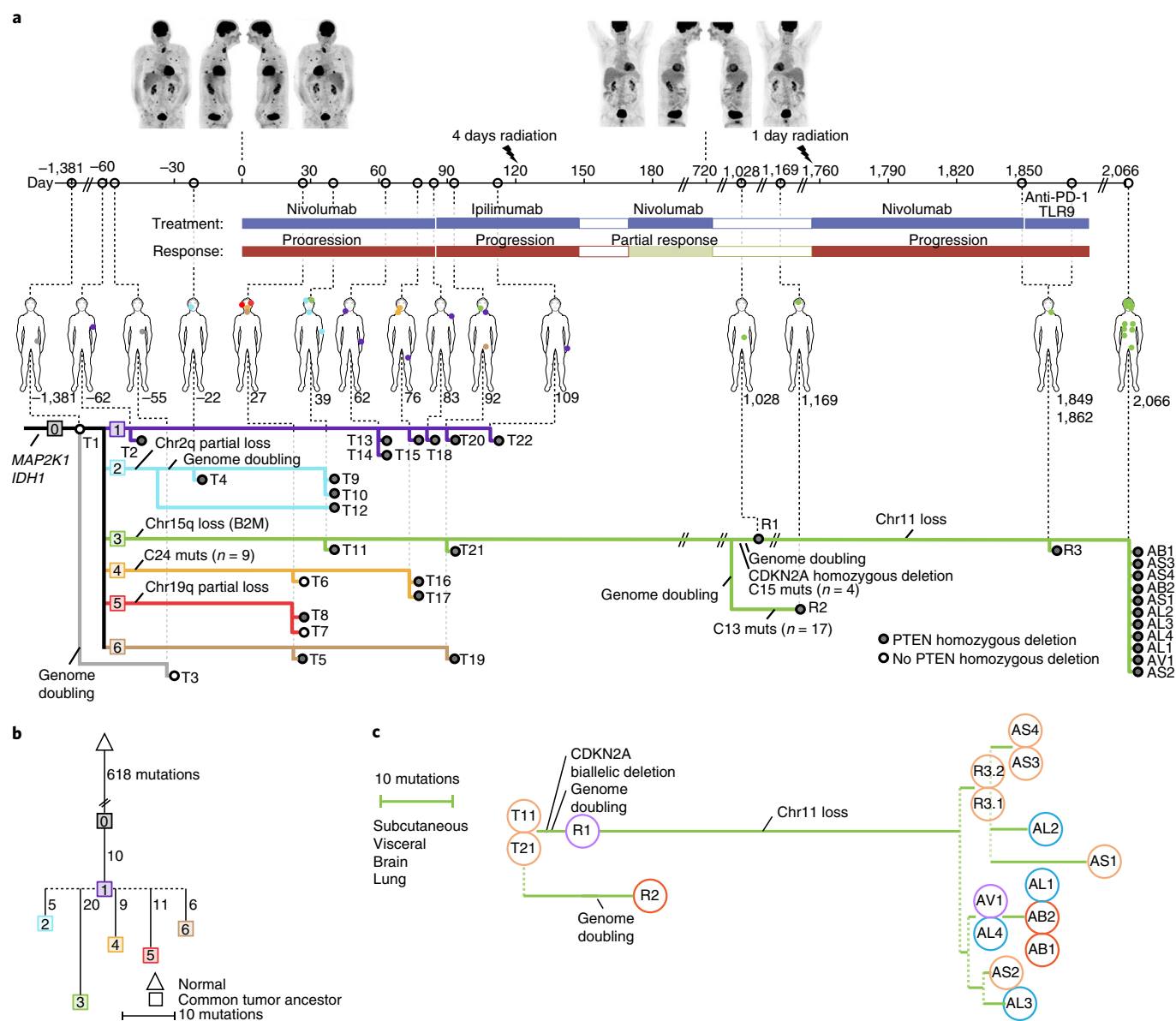
Fig. 1 | Integrated clinical course and phylogenetic characterization of longitudinal tumor biopsies. a, Clinical course (top). Numbers on the timeline indicate days relative to initiation of ICB. Above, positron emission tomography–computed tomography images taken at (1) time of initial metastatic recurrence pre-ICB treatment and (2) completion of 2 years of ICB. Briefly, the patient was a 67-year-old man with stage IIB nodular melanoma treated with wide excision and negative sentinel lymph node biopsies that recurred 2.5 years later with widespread disease to subcutaneous lesions, lungs, lymph nodes and visceral lesions. He was enrolled into a trial of sequential ICB[15] and had a heterogeneous response with overall rapid progressive disease on initial six cycles of nivolumab and again on four cycles of ipilimumab and underwent palliative radiation of bone metastases. Coinciding with maintenance nivolumab (D182), he experienced an abrupt, precipitous response, completing 2 total years of ICB and was considered a complete clinical responder. In the next year, he developed autoimmune nephritis requiring high-dose steroids and subsequently had an isolated jejunal metastasis and occipital brain lesion resected. Two years later, he had widespread metastatic recurrence resistant to subsequent therapy, including re-trial of nivolumab, anti-PD-1 therapy + TLR9 agonist, carboplatin and paclitaxel and died of his disease approximately 1 year after metastatic recurrence. See Methods for full clinical course. Phylogenetic analysis from WES (bottom). Each dot represents a different tumor biopsy (with physical location on the figure above) and each colored line represents a tumor lineage with shared genomic alterations as indicated. We inferred seven different tumor lineages (labeled 0 through 6) pre-existing at treatment initiation. Phylogenies and lineages were inferred using point mutations (muts) and copy-number events (Methods, Extended Data Figs. 4 and 5 and Supplementary Fig. 1). **b**, Phylogenetic relationships between lineages. The most recent common ancestor (MRCA) for each lineage and their relationships were inferred. Distances are based on the number of different mutations, including gained and lost mutations (via deletion of chromosomal segments). **c**, Detailed phylogenetic relationships of lineage 3. The phylogenetic relationships of tumors in the resistant lineage (lineage 3) are depicted, with phylogenetic distance based on the number of gained and lost mutations.

a trial of intralesional TLR9 agonist plus anti-PD-1 and we collected paired pre-treatment and post-treatment (D1,849 and D1,862) biopsies for direct intratumoral comparison of the nonresponsive target tumor (Fig. 3e). The t-CyCIF demonstrated post-treatment increase in immune infiltrate accompanied by an increase in the NGFR^hiPD-L1+ tumor population (Fig. 3f and Extended Data Fig. 9b), with expansion of CD8+ T cells and nonlymphocytic immune cells (CD45+/CD3d−) as a proportion of the immune
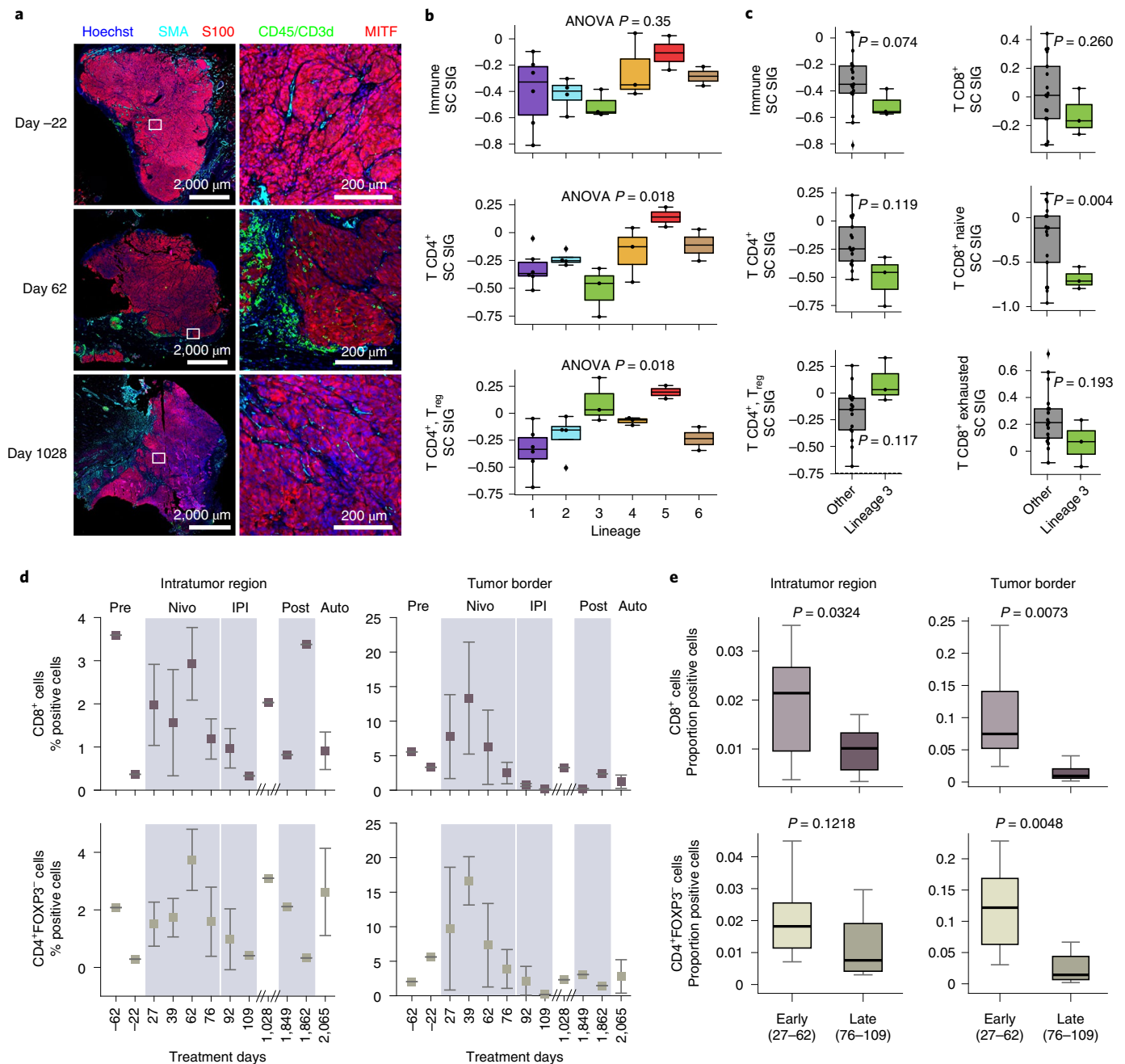
Fig. 2 | Analysis of immune microenvironment by lineage and time. Overall expression of immune cell signatures (from melanoma single-cell RNA-seq[17]) was inferred in 20 tumors with bulk RNA-seq transcriptomes and tested for association with lineage and time post-treatment. Concurrent t-CyCIF-assessed proportion of immune cell subsets from digital imaging and cell classification (Methods). **a**, Representative digital imaging of t-CyCIF. Tumors from pre-treatment (D−22), on-treatment (D62) and post-treatment progression (D1,028) highlight tumor cells (S100 or MITF, red), immune cells (CD45 or CD3d, green) and stromal cells (SMA, cyan). **b**, Expression of selected single-cell-derived immune cell signatures (SC SIG) by lineage. There was no statistically significant association between lineage and expression of overall immune cell signature (one-way ANOVA $P = 0.35$), but there was a statistically significant association with CD4^{+} T cell and CD4^{+} regulatory T cell (T_{reg}) signatures (one-way ANOVA $P = 0.018$, Benjamini–Hochberg false discovery rate $q = 0.09$, both). Number of tumors per lineage, lineage 1 ($n = 6$); lineage 2 ($n = 4$); lineage 3 ($n = 3$); lineage 4 ($n = 3$); lineage 5 ($n = 2$); lineage 6 ($n = 2$). **c**, Overall expression of immune and T cell signatures in resistant lineage (lineage 3) ($n = 3$) versus others ($n = 17$). Observed mean immune and T cell signature scores were lower in lineage 3 tumors (except CD4^{+} regulatory T cells, which were higher). Results were generally not statistically significant given small sample except naive CD8^{+} T cells, unadjusted two-sided Student's t-test $P = 0.004$. **d**, Overall proportion of CD8^{+} (effector) and CD4^{+}/FoxP3^{−} (helper) T cells over time and region. Proportions of immune populations are shown from 34 tumors analyzed using t-CyCIF. Error bars represent s.e.m. **e**, Comparison of immune cell proportions in early versus late on-treatment time points. Early on-treatment (D27–62) ($n = 10$) versus late on-treatment (D76–109) ($n = 8$) tumors compare CD8^{+} (effector) and CD4^{+}/FoxP3^{−} (helper) T cell proportions in intratumoral regions and at tumor border. P values were calculated with unpaired, two-sided Student's t-test and unadjusted for multiple hypotheses. Box plot limits indicate the interquartile range (IQR) (25th to 75th percentiles), with center line indicating the median. Whiskers show value ranges up to $1.5 \times$ IQR above the 75th or below the 25th percentiles, with outliers beyond those ranges shown as individual points.

infiltrate (Fig. 3g; Fisher's exact test $P < 0.001$ for both). Finally, single-cell RNA-seq of the post-treatment tumor biopsy (Fig. 3h) confirmed the presence of an NGFR[hi] tumor population and GSEA (Methods) revealed enrichment of hypoxia, immunostimulatory and immunoregulatory gene sets (tumor necrosis factor-α/transforming growth factor-β), EMT and P53 pathways in NGFR^{hi} tumor cells, whereas gene sets involving oxidative phosphorylation, cell-cycle checkpoints and MYC targets were enriched in the NGFR^{lo} cells (Fig. 3i). Separate single-cell RNA-seq of brain metastasis confirmed differential enrichment of these pathways between NGFR[hi] and NGFR^{lo} tumor cells (Supplementary Fig. 7 and Supplementary Table 2).

To compare differences in tumor and TME between different tumor sites at the same time point, we performed t-CyCIF on 11 rapid autopsy samples (Fig. 4a) and focused on differences in the tumor and microenvironment across the most represented metastatic sites: lung ($n = 4$) and subcutaneous ($n = 4$) metastases. There were no differences in NGFRhi tumor cell proportion or CD8+ cytotoxic or CD4+ T helper populations between lung and subcutaneous sites, but there were higher frequencies of Ki67+ tumor cells in the lung compared to subcutaneous tumors ($P = 0.003$, Fig. 4b). Despite no quantitative differences in NGFR[hi] tumor cell populations between lung and subcutaneous metastatic sites, we observed two different spatial patterns: (1) concentration of NGFR^{hi} cells in the periphery of tumor adjacent to immune cells in subcutaneous metastases; and (2) a more diffuse NGFR[hi] tumor cell distribution throughout the tumor in lung metastases (Fig. 4c,d). Using metrics of polarity and entropy to quantify these observations (Methods), we found that NGFR^{hi} tumor cells had higher polarity and lower entropy in subcutaneous versus lung locations (Student's t-test $P = 0.032$, $P = 0.030$ respectively, Fig. 4e). Consistent with potentially distinct roles in immune cell response and pseudovascularization, there was a closer spatial relationship between NGFR^{hi} tumor cells and cytotoxic and T helper cells in subcutaneous tumors compared to tumors in the lung ($P < 8.2 \times 10^{-11}$, Fig. 4f).

In this study, we report tumor-intrinsic and immune evolutionary dynamics in a patient with melanoma treated with ICB. Using molecular and protein characterization of 37 longitudinal tumor samples we deduced the branched evolutionary structure, mapped the timing of immune escape, analyzed the immune microenvironment and demonstrated phenotypic selection for a less-differentiated, NGFR[hi] program in tumor cells. Seven genomic lineages were inferred, suggesting marked tumor heterogeneity at the start of therapy[36] and persisting through initial therapy. Multiple resistance-associated alterations were identified, including *PTEN* loss[6–8], genome doubling with increased aneuploidy[12,13] and loss of

antigen presentation[9,10]. After ICB, early recurrences demonstrated acquisition of multiple resistance alterations, arising out of the lineage with 15q deletion (including *B2M*) that harbored a PTEN homozygous deletion and additional genomic alterations, including genome doubling and biallelic CDKN2A loss. This supports the concept of immune pruning of susceptible clones[37,38], propagation of clones with intrinsic (and multiple) immune-evasive adaptations and suggests the insufficiency of any single alteration to intrinsically support survival and outgrowth. Notably, the clone comprising early brain metastasis was an evolutionary dead end, with no subsequent recurrence after resection and radiation, whereas the early bowel metastasis clone was the ancestor to all subsequent resistant metastases (including brain metastases at rapid autopsy), supporting the possibility of disease eradication with aggressive treatment of oligometastases.

This patient's clinical course was unusual, with a long interval between primary tumor and first metastasis, followed by rapid tumor growth and heterogeneous responses to ICB and abrupt clinical complete response for which the trigger was unknown. Preceding complete response was initiation of CTLA-4 checkpoint inhibitors and palliative radiation, suggesting the contribution of an abscopal effect. Additionally, the features leading to the resistant clone arising from lineage 3 (with chromosome 15q LOH including B2M) are not completely characterized. While RNA-seq analysis suggests decreased MHC-I expression in lineage 3 tumors (t-test $P = 0.01$, Extended Data Fig. 10a), there was not complete loss via t-CyCIF with continued tumoral HLA-A protein expression. An alternate hypothesis is that mutations on the deleted segment of chromosome 15q generated immunogenic neoantigens. We see evidence of decreased expression of genes coding neoantigens in lineage 3 tumors and over time (Extended Data Fig. 10b). Finally, early recurrences occurred after steroid treatment for autoimmune nephritis followed by indolent disease progression for 2 years transitioning to later recurrence of more aggressive, rapidly therapy-refractory disease, suggesting that causes of persistence of the resistant clone and subsequent progression are multifactorial.
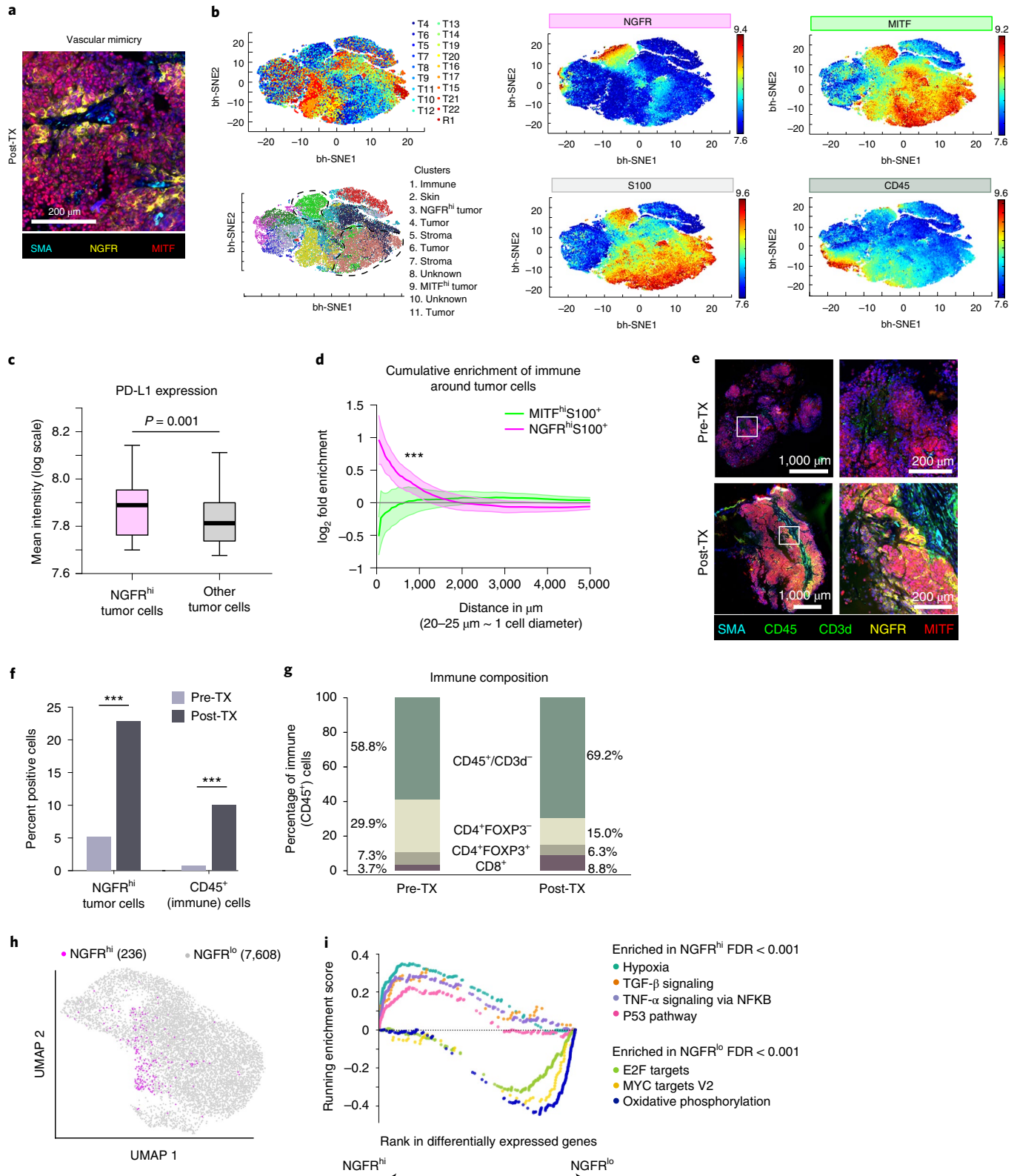
Previous studies have defined an NGFR[hi] program within a subset of melanoma cells in association with de-differentiation[35], increased invasiveness and decreased proliferation[16] and demonstrated functional relevance to targeted therapy resistance[15,39,40] and immunotherapy in vitro/in vivo[41]. However, a more granular assessment of the NGFR[hi] phenotype within ICB-treated patients has not been demonstrated. Here, we find that the melanoma NGFR[hi] state is characterized by high PD-L1 expression and close spatial association with immune cells, suggesting a role in tumor–immune interactions, consistent with recent in vitro studies demonstrating

---

Fig. 3 | Spatial and immune correlates of NGFR^{hi} tumor cells. a, t-CyCIF vasculogenic mimicry of tumor cells. t-CyCIF of R3.2 (post-treatment lesion, D1,862). TX, treatment. **b**, t-CyCIF single-cell dimensionality reduction representation using t-stochastic neighbor embedded (t-SNE) algorithm. Cells from 19 tumors (D−55 through D1,028) highlighting (counter-clockwise from top left): cells from different tumors; inferred clusters using Gaussian mixture models (GMMs); tumor cells (S100+); immune cells (CD45+); MITF^{hi} cells and NGFR^{hi} cells. **c**, PD-L1 expression in NGFR^{hi} tumor cells ($n = 10,386$) versus other tumor cells ($n = 124,763$; two-sided Student's t-test $P = 0.001$, unadjusted). **d**, Spatial proximity: NGFR[hi]/MITF^{hi} tumor cells to immune cells. Shaded regions cover two × s.e.m. of log fold enrichment of immune cells within a given radius. At <1,000 μm (~40–50 cell diameters), immune cells enrich in proximity to NGFR^{hi} tumor cells relative to all tumor cells, but not MITF^{hi} tumor cells (exponential regression z-test, $P < 3 \times 10^{-40}$). **e**, t-CyCIF from same tumor pre- (R3.1, D1,849) and post- (R3.2, D1862) treatment with TLR9 agonist plus aPD-1. Immune cells (CD45 or CD3d, green), MITF^{hi} tumor cells (red), NGFR^{hi} tumor cells (NGFR and S100, yellow) and stroma (SMA, cyan). **f**, Proportion of NGFR[hi]S100+ tumor cells ($P = 8.3991 \times 10^{-323}$) and CD45+ immune cells ($P = 5.1214 \times 10^{-62}$) in pre-/post-treatment tumors (two-tailed Fisher's exact test, unadjusted). **g**, Immune cell composition in pre- and post-treatment tumors. Proportions of immune subsets inferred using t-CyCIF. There are post-treatment increases in proportion of CD8+ T cells ($P = 4.614 \times 10^{-76}$) and non-T cell immune cell subsets ($P = 3.4725 \times 10^{-43}$, two-tailed Fisher's exact test, unadjusted). **h**, Uniform manifold approximation and projection (UMAP) of single-cell RNA-seq of tumor cells from R3.2 (post-treatment D1,862). NGFR^{hi} tumor cells are highlighted using an NGFR program signature. **i**, GSEA of NGFR[hi] versus NGFR^{lo} tumor cells using Hallmark gene sets[46]. Each point represents a gene within a gene set. Results from R3.2 (post-treatment D1,862) are shown and concordant with R2 (brain metastasis D1,169) (Supplementary Fig. 6 and Supplementary Table 2). Box plot limits indicate IQR (25th to 75th percentiles) with center line indicating the median. Whiskers show value ranges up to 1.5 × IQR above the 75th or below the 25th percentiles, with outliers shown as individual points. *$P < 0.05$; **$P < 0.01$; ***$P < 0.001$. FDR, false discovery rate; TGF, transforming growth factor; TNF, tumor necrosis factor.

resistance to T cell killing in NGFR^{hi} tumor cells[41]. We observe enrichment of hypoxia pathways in NGFR^{hi} tumor cells and cytoarchitecture consistent with vascular mimicry[34,42], suggesting a potential role in increasing circulation to the tumor[34], regulating immune cell entry[43] and nominating these cells as targets for therapeutic intervention. Our analysis describes distinct NGFR[hi] tumor cell

distribution patterns in lung versus subcutaneous metastatic sites, potentially reflecting site-specific heterogeneity in tumor–immune interactions.

Whether the evolutionary dynamics of this patient's tumor reflect the broader cohort of melanoma treated with ICB must be assessed in larger cohorts representing all melanoma genotypes and
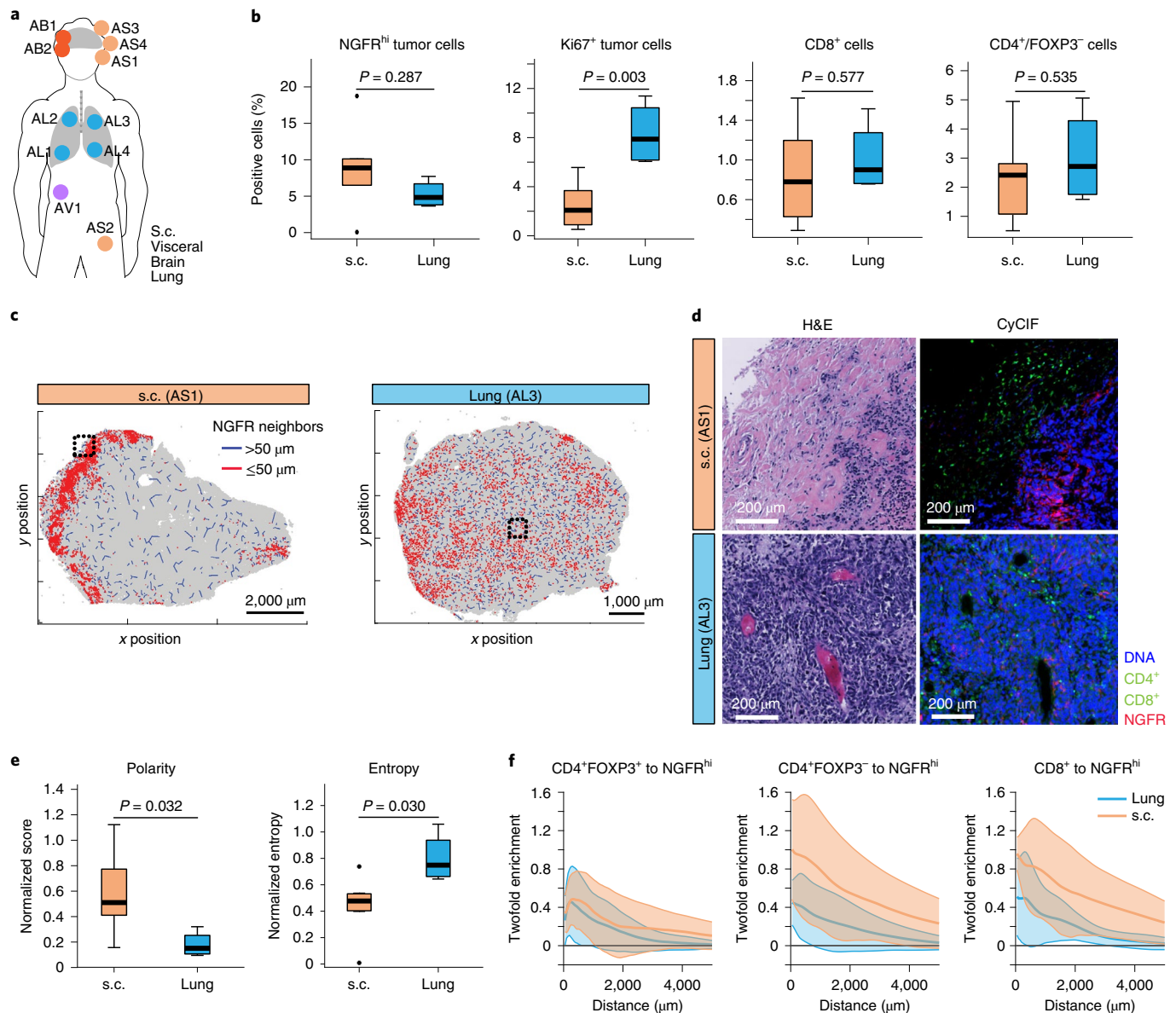

Fig. a–i

Fig. 4 | NGFR^hi tumor and immune microenvironment by metastatic sites. a, Autopsy biopsies from metastases in lung (n = 4), subcutaneous (n = 4), brain (n = 2) and adrenals (n = 1). s.c., subcutaneous. **b**, t-CyCIF quantification of tumor and immune populations. NGFR^hi or Ki67+ tumor cells were calculated and percentage of positive cells (over all cells quantified) are represented as box plots (left). CD8a+ (cytotoxic T cells) and CD4+/FoxP3− (helper T cells) were quantified (right). Unadjusted P values were calculated with two-sided Student's t-tests between lung or s.c. sites. **c**, Macro-scale patterns of NGFR distribution in representative examples of lung and skin metastases. Red lines represent a NGFR^hi tumor neighbor within 50 μm, blue lines indicate neighbor >50 μm distant. **d**, Exemplar H&E and t-CyCIF images of tumors from different anatomic locations (lung versus s.c.). Four-channel CyCIF images (blue, DNA; green, CD8a, CD4; red, NGFR) (right) and corresponding H&E (left). H&E, hematoxylin and eosin. **e**, Polarity and entropy of NGFR^hi cells in lung versus s.c. metastases. We found higher polarity in s.c. lesions (P = 0.032) and higher entropy in the lung lesions (P = 0.030) (two-sided Student's t-test, unadjusted) (Methods). **f**, Spatial association of NGFR^hi tumor cells with immune cell populations. The log fold enrichment of immune cells within a given radius of NGFR^hi tumor cells relative to all tumor cells is shown for s.c. and lung lesions. Shaded regions cover 2 × s.e.m. of log fold enrichment. Immune cells are enriched in the proximity of NGFR^hi tumor cells in both lung and s.c. locations (exponential regression z-test CD4+FOXP3+ (lung, $P = 3.2 \times 10^{-47}$; s.c., $P = 6.4 \times 10^{-50}$); CD4+FOXP3− (lung, $P = 5.5 \times 10^{-50}$; s.c., $P = 7.8 \times 10^{-73}$); CD8+ (lung, $P = 2.3 \times 10^{-66}$; s.c., $P = 3.4 \times 10^{-96}$)). However, s.c. samples had stronger enrichment of CD4+FOXP3− and CD8+ cells (exponential regression z-test, CD8+, $P = 8.2 \times 10^{-11}$; CD4+FOXP3−, $P = 9.5 \times 10^{-18}$) but not CD4+FOXP3+ cells (P = 0.85) compared to lung samples. Box plot limits indicate IQR (25th to 75th percentiles), with center line indicating the median. Whiskers show value ranges up to 1.5 × IQR above 75th or below 25th percentiles, with outliers shown as individual points.

reflecting the breadth of clinical heterogeneity; however, this study provides molecular insight into the development of immunotherapy resistance and integrates longitudinal sequencing and imaging approaches to thoroughly define tumor and immune cell interactions. Further efforts are ongoing, including integrating analysis

of plasma/peripheral blood mononuclear cells[44,45] in parallel with deep molecular analysis of the tumor, potentially affording a less invasive means of tumor/immune assessment longitudinally; and integration of additional modalities (for example epigenetic sequencing) at different scales (bulk, single cell) to dissect longitudinal

intrapatient heterogeneity. We anticipate that clinically contextualized, longitudinal multimodal molecular analyses to dissect changes in the tumor and tumor microenvironment under therapy will enable deeper understanding of the evolution of resistance and tumor heterogeneity and improve outcomes by identifying new targets and informing rational combination therapies.

Online content

Any methods, additional references, Nature Research reporting summaries, source data, extended data, supplementary information, acknowledgements, peer review information; details of author contributions and competing interests; and statements of data and code availability are available at https://doi.org/10.1038/s41591-021-01331-8.

References

1. Wolchok, J. D. et al. Overall survival with combined nivolumab and ipilimumab in advanced melanoma. *N. Engl. J. Med.* **377**, 1345–1356 (2017).
2. Robert, C. et al. Pembrolizumab versus ipilimumab in advanced melanoma. *N. Engl. J. Med.* **372**, 2521–2532 (2015).
3. Larkin, J. et al. Five-year survival with combined nivolumab and ipilimumab in advanced melanoma. *N. Engl. J. Med.* **381**, 1535–1546 (2019).
4. Sharma, P., Hu-Lieskovan, S., Wargo, J. A. & Ribas, A. Primary, adaptive, and acquired resistance to cancer immunotherapy. *Cell* **168**, 707–723 (2017).
5. Spranger, S., Bao, R. & Gajewski, T. F. Melanoma-intrinsic β-catenin signalling prevents anti-tumour immunity. *Nature* **523**, 231 (2015).
6. George, S. et al. Loss of PTEN is associated with resistance to anti-PD-1 checkpoint blockade therapy in metastatic uterine leiomyosarcoma. *Immunity* **46**, 197–204 (2017).
7. Xiao, Q. et al. DKK2 imparts tumor immunity evasion through β-catenin-independent suppression of cytotoxic immune-cell activation. *Nat. Med.* **24**, 262–270 (2018).
8. Peng, W. et al. Loss of PTEN promotes resistance to T cell-mediated immunotherapy. *Cancer Discov.* **6**, 202–216 (2016).
9. Zaretsky, J. M. et al. Mutations associated with acquired resistance to PD-1 blockade in melanoma. *N. Engl. J. Med.* **375**, 819–829 (2016).
10. Sade-Feldman, M. et al. Resistance to checkpoint blockade therapy through inactivation of antigen presentation. *Nat Commun.* **8**, 1136 (2017).
11. Gao, J. et al. Loss of IFN-γ pathway genes in tumor cells as a mechanism of resistance to anti-CTLA-4 therapy. *Cell* **167**, 397–404 (2016).
12. Davoli, T., Uno, H., Wooten, E. C. & Elledge S. J. Tumor aneuploidy correlates with markers of immune evasion and with reduced response to immunotherapy. *Science* https://doi.org/10.1126/science.aaf8399 (2017).
13. Roh, W. et al. Integrated molecular analysis of tumor biopsies on sequential CTLA-4 and PD-1 blockade reveals markers of response and resistance. *Sci. Transl. Med.* https://doi.org/10.1126/scitranslmed.aah3560 (2017).
14. Goel, S. et al. CDK4/6 inhibition triggers anti-tumour immunity. *Nature* **548**, 471 (2017).
15. Rambow, F. et al. Toward minimal residual disease-directed therapy in melanoma. *Cell* **174**, 843–855 (2018).
16. Restivo, G. et al. The low affinity neurotrophin receptor CD271 regulates phenotype switching in melanoma. *Nat. Commun.* **8**, 1988 (2017).
17. Jerby-Arnon, L. et al. A cancer cell program promotes T cell exclusion and resistance to checkpoint blockade. *Cell* **175**, 984–997 (2018).
18. Burrell, R. A., McGranahan, N., Bartek, J. & Swanton, C. The causes and consequences of genetic heterogeneity in cancer evolution. *Nature* **501**, 338–345 (2013).
19. Gerlinger, M. et al. Intratumor heterogeneity and branched evolution revealed by multiregion sequencing. *N. Engl. J. Med.* **366**, 883–892 (2012).
20. Jamal-Hanjani, M. et al. Tracking the evolution of non–small-cell lung cancer. *N. Engl. J. Med.* **376**, 2109–2121 (2017).
21. Faltas, B. M. et al. Clonal evolution of chemotherapy-resistant urothelial carcinoma. *Nat. Genet.* https://doi.org/10.1038/ng.3692 (2016).
22. Andor, N. et al. Pan-cancer analysis of the extent and consequences of intratumor heterogeneity. *Nat. Med.* **22**, 105–113 (2016).
23. Ding, L. et al. Clonal architectures and driver mutations in metastatic melanomas. *PLoS ONE* **9**, e111153 (2014).
24. Jiménez-Sánchez, A. et al. Heterogeneous tumor-immune microenvironments among differentially growing metastases in an ovarian cancer patient. *Cell* **170**, 927–938 (2017).
25. Liu, D. et al. Mutational patterns in chemotherapy resistant muscle-invasive bladder cancer. *Nat. Commun.* **8**, 2193 (2017).
26. Juric, D. et al. Convergent loss of PTEN leads to clinical resistance to a PI(3) Kα inhibitor. *Nature* **518**, 240–244 (2015).
27. Chen, P.-L. et al. Analysis of immune signatures in longitudinal tumor samples yields insight into biomarkers of response and mechanisms of resistance to immune checkpoint blockade. *Cancer Discov.* **6**, 827–837 (2016).
28. Edwards, J. et al. Prevalence and cellular distribution of novel immune checkpoint targets across longitudinal specimens in treatment-naive melanoma patients: implications for clinical trials. *Clin. Cancer Res.* **25**, 3247–3258 (2019).
29. Dewhurst, S. M. et al. Tolerance of whole-genome doubling propagates chromosomal instability and accelerates cancer genome evolution. *Cancer Discov.* **4**, 175–185 (2014).
30. The Cancer Genome Atlas. Genomic classification of cutaneous melanoma. *Cell* **161**, 1681–1696 (2015).
31. Liu, D. et al. Integrative molecular and clinical modeling of clinical outcomes to PD1 blockade in patients with metastatic melanoma. *Nat. Med.* **25**, 1916–1927 (2019).
32. Barbie, D. A. et al. Systematic RNA interference reveals that oncogenic KRAS-driven cancers require TBK1. *Nature* **462**, 108–112 (2009).
33. Liberzon, A. et al. The molecular signatures database hallmark gene set collection. *Cell Syst.* **1**, 417–425 (2015).
34. Maniotis, A. J. et al. Vascular channel formation by human melanoma cells in vivo and in vitro: vasculogenic mimicry. *Am. J. Pathol.* **155**, 739–752 (1999).
35. Landsberg, J. et al. Melanomas resist T-cell therapy through inflammation-induced reversible dedifferentiation. *Nature* **490**, 412–416 (2012).
36. Sottoriva, A. et al. A Big Bang model of human colorectal tumor growth. *Nat. Genet.* **47**, 209–216 (2015).
37. Rooney, M. S., Shukla, S. A., Wu, C. J., Getz, G. & Hacohen, N. Molecular and genetic properties of tumors associated with local immune cytolytic activity. *Cell* **160**, 48–61 (2015).
38. Riaz, N. et al. Tumor and microenvironment evolution during immunotherapy with nivolumab. *Cell* https://doi.org/10.1016/j.cell.2017.09.028 (2017).
39. Lehraiki, A. et al. Increased CD271 expression by the NF-κB pathway promotes melanoma cell survival and drives acquired resistance to BRAF inhibitor vemurafenib. *Cell Discov.* **1**, 1–13 (2015).
40. Shaffer, S. M. et al. Rare cell variability and drug-induced reprogramming as a mode of cancer drug resistance. *Nature* **546**, 431–435 (2017).
41. Boshuizen, J. et al. Reversal of pre-existing NGFR-driven tumor and immune therapy resistance. *Nat. Commun.* **11**, 3946 (2020).
42. Valyi-Nagy, K., Kormos, B., Ali, M., Shukla, D. & Valyi-Nagy, T. Stem cell marker CD271 is expressed by vasculogenic mimicry-forming uveal melanoma cells in three-dimensional cultures. *Mol. Vis.* **18**, 588–592 (2012).
43. Tan, L. Y. et al. Control of immune cell entry through the tumour vasculature: a missing link in optimising melanoma immunotherapy? *Clin. Transl. Immunol.* **6**, e134 (2017).
44. Shi, A. et al. Plasma-derived extracellular vesicle analysis and deconvolution enable prediction and tracking of melanoma checkpoint blockade outcome. *Sci. Adv.* **6**, eabb3461 (2020).
45. Marsavela, G. et al. Circulating tumor DNA predicts outcome from first-, but not second-line treatment and identifies melanoma patients who may benefit from combination immunotherapy. *Clin. Cancer Res.* **26**, 5926–5933 (2020).
46. Langmead, B. & Salzberg, S. L. Fast gapped-read alignment with Bowtie 2. *Nat. Methods* **9**, 357–359 (2012).

Methods

Patient samples. Institutional Review Board approval was obtained before study enrollment and written informed consent was obtained from the patient for the collection of tissue and blood samples and use of medical imaging for research and genomic profiling, as approved by the Dana-Farber/Harvard Cancer Center Institutional Review Board (DF/HCC Protocol 11-181). Response was assessed using modified RECIST 1.1 criteria and restaging scans were performed at least every 3 months to assess response and progression.

Clinical history and sample context. A 67-year-old man with stage IIB nodular melanoma treated with wide excision and negative sentinel lymph node biopsies recurred 2.5 years later and staging positron emission tomography–computed tomography images showed widespread disease, including lymph node, lungs, subcutaneous and visceral lesions. He enrolled in a phase 2 trial of sequential ICB[15] and received nivolumab then ipilimumab then maintenance nivolumab. After six cycles of nivolumab, he had heterogeneous response to ICB (RECIST 1.1; PD, −17%) with overall rapid progression. He continued to progress over four cycles of ipilimumab and underwent palliative radiation of bone metastases. Coinciding with maintenance nivolumab (D182), he experienced an abrupt, precipitous response. Restaging scans (D221) demonstrated a partial response (RECIST 1.1, −45%) with continued disease regression. He completed 2 total years of ICB with excellent radiographic response (D753, RECIST 1.1, −73%) and was considered a complete clinical responder (only residual scar on imaging). Three months after trial completion (D831), he developed autoimmune nephritis requiring high-dose steroids. Six months later (D1,015), imaging revealed an isolated jejunal metastasis that was resected. Five months later, imaging demonstrated a new occipital brain lesion that was resected (D1,169) with post-operative radiation therapy. He then did well with no recurrence until a year and a half later when he had widespread metastatic recurrence. He resumed nivolumab, but progressed on therapy. He transitioned to a clinical trial of anti-PD-1 therapy + TLR9 agonist (D1,850) but progressed. Despite subsequent radiation, carboplatin and paclitaxel, the patient died of his disease approximately 1 year after metastatic recurrence and almost 6 years from initiation of ICB.

Multiple rounds of palliative resection of subcutaneous lesions were performed during the early on-treatment phase of his clinical course and ultimately biopsies from 37 tumors underwent molecular characterization from the original primary ($n = 1$), pre-treatment ($n = 3$), on-treatment ($n = 18$) and post-treatment progression ($n = 15$) time points, spanning 9 years.

DNA/RNA extraction and exome sequencing. DNA extraction, whole-exome library preparation and sequencing was performed for samples as previously described[25,47]. Slides were cut from formalin-fixed and paraffin-embedded (FFPE) blocks and examined by a board-certified pathologist to select high-density cancer foci and ensure high purity of cancer DNA. Biopsy cores were taken from the corresponding tissue block for DNA/RNA extraction. DNA and RNA extraction was performed using QIAGEN AllPrep DNA/RNA Mini kit (no. 51306) and stored at −20 °C. Whole-exome capture libraries were constructed from 100 ng of DNA from tumor and normal tissues after sample shearing, end repair and phosphorylation and ligation to barcoded sequencing adaptors. Ligated DNA was size selected for lengths between 200–350 bp and subjected to exonic hybrid capture using Illumina library preps. The sample was multiplexed and sequenced using Illumina HiSeq technology. The Illumina exome uses Illumina's in-solution DNA probe-based hybrid selection method that uses similar principles as the Broad Institute-Agilent Technologies developed in-solution RNA probe-based hybrid selection method[48,49] to generate Illumina exome sequencing libraries.

Total RNA was assessed for quality using the Caliper LabChip GX2. The percentage of fragments with a size greater than 200 nt (DV200) was calculated using software. An aliquot of 200 ng of RNA was used as the input for first-strand complementary DNA synthesis using Illumina's TruSeq RNA Access Library Prep kit. Synthesis of the second strand of cDNA was followed by indexed adaptor ligation. Subsequent PCR amplification enriched for adapted fragments. The amplified libraries were quantified using an automated PicoGreen assay.

A total of 200 ng of each cDNA library, not including controls, were combined into four-plex pools. Capture probes that target the exome were added and hybridized for recommended time. Following hybridization, streptavidin magnetic beads were used to capture the library-bound probes from the previous step. Two wash steps effectively remove any nonspecifically bound products. These same hybridization, capture and wash steps are repeated to assure high specificity. A second round of amplification enriches the captured libraries. After enrichment the libraries were quantified with qPCR using the KAPA Library Quantification kit for Illumina Sequencing Platforms and then pooled equimolarly. The entire process was in 96-well format and all pipetting was performed by either Agilent Bravo or Hamilton Starlet.

Pooled libraries were normalized to 2 nM and denatured using 0.2 N NaOH before sequencing. Flowcell cluster amplification and sequencing were performed according to the manufacturer's protocols using either the HiSeq 2000 v3 or HiSeq 2500. Each run was a 76-bp paired-end with a dual eight-base index barcode read. Data were analyzed using the Broad Picard Pipeline, which includes de-multiplexing and data aggregation.

Quality control and variant calling. Initial exome sequence data processing and analysis were performed using a customized version of the Getz Lab WES analysis pipeline (https://portal.firecloud.org/#methods/getzlab/CGA_WES_Characterization_Pipeline_v0.1_Dec2018/) at the Broad Institute. After alignment from the Broad Picard Pipeline, BAM files were uploaded into the Terra infrastructure (https://app.terra.bio), which managed intermediate analysis files executed by analysis pipelines.

Out of an initial 44 samples (43 tumor + 1 blood normal), all passed coverage (>50× mean target coverage) and contamination estimation[50] (<5%) thresholds except the primary tumor (T1, D−1,381, 34× mean target coverage, 13% contamination), which we kept due to its importance in phylogenetic analysis. We removed 6 tumors due to low tumor purity (<10% tumor cells and no matched mutations in significantly mutated genes[51,52]), yielding 37 total tumor samples + 1 matched blood normal for analysis. Supplementary Table 1 shows sequencing characteristics.

The MuTect algorithm[53] was applied to identify somatic single-nucleotide variants in targeted exons. Strelka[54] was applied to identify small insertions or deletions. Alterations were annotated using Oncotator[55]. Filters were applied to detect and remove known artifacts and germline variants, including DNA oxidation during sequencing[56].

Copy-number variants. Total copy-number alterations for individual tumors were inferred using adaptations of a binary segmentation algorithm[57,58] (CapSeg) comparing fractional exon coverage for tumor segments to a panel of normal samples, generating exomic segments and segment copy number. Copy-number data were inspected visually and manually for focal amplifications and deletions and genes were annotated with Oncotator[55]. For allelic copy numbers, heterozygous single-nucleotide polymorphisms were identified and integrated with the binary segmentation algorithm (Allelic CapSeg) and further adjusted for tumor purity and ploidy[59]. We then called allelic amplifications and deletions, following previously described criteria[60] integrating segment focality and the revised allelic copy number.

Purity and ploidy. Purity and ploidy was estimated using the ABSOLUTE algorithm[59], which integrates variant allele frequency distributions and copy-number variants (CNVs) to estimate absolute tumor purity and ploidy and infer cancer cell fraction (CCF), the proportion of cancer cells in the sample which contain each mutation. Post-purity and ploidy-corrected allelic segments were used to estimate allelic copy-number estimates.

Aneuploidy calculation. We used an adaptation of the weighted Genome Instability Index[29,61] to calculate a measure of genomic aneuploidy for each sample. First, we used the allelic segment output to determine the median genomic allelic copy number (for example, one for nongenome-doubled samples and two for genome-doubled samples), semantically the 50th percentile of allelic copy number for base pairs across the genome. Then, to calculate genomic aneuploidy, we estimated the proportion of the genome with a different allelic copy number from this median.

Phylogenetic analysis. Two complementary approaches were taken to perform phylogenetic analyses: PyClone[62] and PhylogicNDT[63].

A comprehensive list of all called point mutations and small insertion/deletions found in any tumor sample was generated. For each tumor sample, the number of alt and reference reads, estimated CCF and purity and ploidy-corrected minor and major copy number at each mutation locus was generated. PyClone[62] (v.0.13.1), a Bayesian clustering method for grouping mutations into clonal structures accounting for tumor purity and allelic copy numbers, was then used to generate clusters of mutations and their estimated CCF for each sample, given the described mutation inputs and tumor purity. The following default parameters were used:

```
base_measure_params: {alpha: 1, beta: 1}
beta_binomial_precision_params:
    prior: {rate: 0.001, shape: 1.0}
    proposal: {precision: 0.01}
    value: 1,000
concentration:
    prior: {rate: 0.001, shape: 1.0}
    value: 1.0
density: pyclone_beta_binomial
init_method: disconnected
num_iters: 10,000
```

A total of 31 clusters were inferred. After filtering for clusters with more than three mutations, 23 clusters remained (Extended Data Fig. 4a). Three informative patterns emerged:

(1) Clusters with CCF ~1 in all tumors (C2, C4 and C5). Three clusters representing a total of 548 mutations were found at ≥0.6 CCF in all samples (Supplementary Fig. 5a) and likely collectively represent the ancestral clone.
(2) Clusters with CCF ~0 in most tumors and ~1 in a few tumors (C26, C16 and C10; Supplementary Fig. 1d,f and Extended Data Fig. 4c), suggesting a common ancestor for tumors containing these clusters.

(3) Clusters with CCF ~1 in most tumors and 0 in a few tumors (C22, C14 and C8; Extended Data Fig. 4b and Supplementary Fig. 1c,e), with mutations found in the same chromosomal segment, suggesting a common ancestor with deletion of the chromosomal segment containing the cluster mutations for tumors with inferred CCF of 0.

Hierarchical clustering was then performed using Seaborn's clustermap method[21–23] (default clustering using Euclidean distance and the nearest point algorithm for linkage between clusters) (Extended Data Fig. 5a) and seven lineages were inferred. Reassuringly, CNVs (that were not used to generate the lineages) were consistent with the inferred lineages, for example lineage 3 was inferred by lacking C14 composed of 20 mutations in chromosome 15q (Extended Data Fig. 4b) and all tumors in this lineage had a corresponding 15q LOH (Extended Data Fig. 3). Similarly, lineage 5 lacks C8 composed of 11 mutations in a segment of chromosome 19q (Supplementary Fig. 1e), which is inferred as lost in the tumors in lineage 5 (Extended Data Fig. 3). The four tumors (T4, T9, T10 and T12) in lineage 2 shared loss of chromosome 2q mutations (Supplementary Fig. 1c) and had an inferred partial deletion of chromosome 2q. Three of these tumors (T4, T9 and T10) also shared additional acquired mutations as well as a genome-doubling event.

In parallel, we used PhylogicNDT[63] to reconstruct the phylogeny of metastases from DNA sequencing data and inferred cell fractions. PhylogicNDT implements a multidimensional Dirichlet process to jointly estimate cell population structure and genetic phylogeny across all samples, taking copy-number profiles, purity values and joint mutational calls. In our case, we used the posterior distribution on CCF values associated with each mutation (taking into account purity and copy-number profiles using ABSOLUTE[59]). PhylogicNDT Cluster and BuildTree were run on data from selected subsets of samples with the following default parameters: -rb -ni 2,000, -seed 0.

Tumor lineages defined by the PyClone/hierarchical clustering approach were reproduced in phylogenetic tree(s) inferred by PhylogicNDT (Supplementary Fig. 8a,b). The inferred phylogenetic structure of tumors within each lineage is shown in Supplementary Fig. 8c. We extracted inferred mutation patterns characterizing the MRCA of each lineage and used these ancestral patterns to infer the history of early lineage divergence (Fig. 1b)

Immune deconvolution from bulk transcriptomic sequencing. For RNA-seq, we utilized RSEM[64] to quantify transcripts per kilobase million (TPM), fragments per kilobase million (FPKM) and reads per kilobase million (RPKM) levels with bowtie2 (ref. [46]) as the mapper and hg19 as reference genome using default mapping parameters.

We inferred overall expression of 13 immune cell signatures derived from single-cell RNA-seq in melanoma samples as previously described[17]: an overall immune cell signature ('IMMUNE'), a general T cell signature ('T.CELL'), B cell signature ('B.CELL'), different T cell lineages and functional subgroups ('T.CD4', 'T.CD8', 'T.CD4.TREG', 'T.CD8.NAIVE', 'T.CD8.CYTOTOXIC', 'T.CD4. NAIVE', 'T.CD8.EXHAUSTED' and 'T.CD4.EXHAUSTED'), NK cells ('NK') and macrophages ('MACROPHAGE'). Briefly, genes in these signatures were derived by examining genes most distinct to those cell types compared to all other cells in single-cell samples in an unbiased fashion with subsequent expert curation. Overall expression was determined as an averaged normalized score of genes within each gene set; for each tumor. Gene expression was scored based on its normalized expression within the cohort of tumors. Details of signature derivation, scoring and code are available as previously described[17].

Neoantigen inference. Neoantigen prediction was run using Polysolver[65] to determine the patient's human leukocyte antigen types from the blood normal sample. Neoantigen predictions were made using NetMHCPan 4.0 (ref. [66]) from called mutations in each tumor and a threshold for binding affinity of <500 nM, within the framework of the pVAC-seq[67] pipeline.

Multiplexed immunofluorescence. FFPE slides were cut at 5 μm thickness and mounted on a glass slide at the Pathology Core of Massachusetts General Hospital. Due to the extension of sample collection across treatments of the patient, FFPE samples were processed in three batches, as indicated in Supplementary Table 1. We used a recently described method, t-CyCIF, for multiplexed immunofluorescence[68]. In t-CyCIF, single-cell resolution imaging of multiple antigens on the same FFPE slide is achieved by an iterative process that includes staining, image acquisition (and storage) and inactivation of fluorophores, which encompasses a cycle. This cycle is repeated until all images are registered and signal intensities are stacked for individual cells for proteins of interest. Briefly, dewaxing, rehydration and pre-staining were performed on a Leica Bond RX automated stainer using settings described by Lin and colleagues[69]. Blocking was performed using Odyssey blocking buffer (LI-COR, cat. no. 927401). To determine nonspecific binding, FFPE slides were stained with three secondary antibodies conjugated with Alexa-647 anti-mouse (Invitrogen, cat. no. A-21236), Alexa-555 anti-goat (Invitrogen, cat. no. A-21432) and Alexa-488 anti-rabbit (Invitrogen, cat. no. A-11034), followed by nuclear staining using Hoechst 33342 (Life Technologies, cat. no. H3570). For t-CyCIF, fluorophore-conjugated antibodies binding to S100 (Abcam, cat. no. 207367), MITF (Abcam, cat. no. 3201), MHC-I (Abcam, cat. no. 199837), CD3 (Dako, cat. no. A0452), phospho-RB (Santa Cruz, cat. no. 16670)

and Ki67 (CST, cat. no. 11882) (Supplementary Data Table 3) were diluted in Odyssey blocking buffer and incubated for ~12 h at 4 °C in a moisture chamber, followed by washing in 1× phosphate-buffered saline (PBS) four times. Additional antibody information and dilutions used can be found in Supplementary Table 3. Following imaging, fluorophores were inactivated in 4.5% H$_2$O$_2$ and 24 mM NaOH in PBS for 1 h at room temperature in the presence of white light and washed four times in 1× PBS. Imaging was performed on a CyteFinder slide scanning fluorescence microscope (RareCyte) using a ×10 objective (for batch 1) and ×20 objective (for batch 2 and 3). Background subtraction was performed using the previously established rolling ball algorithm (with a 50-pixel radius) in ImageJ[68]. To obtain intensity values for single cells, images were segmented using a previously described[69] Watershed algorithm based on nuclear staining by Hoechst 33342. To generate virtual hyper-stacked images, transformed coordinates were applied to images from four-channel imaging of each CyCIF cycle. The region of interest was defined as tissue with positive S100 staining and immediately adjacent normal tissue. Single-cell intensity distributions are shown as log mean intensity values (x axis) and cell count (y axis). Additional details on used scripts and protocols can be found on http://www.cycif.org/.

Gating and clustering of single-cell data using multiplex immunofluorescence. Single-cell data for given markers were gated using one-dimensional GMM, with the first mode considered as the negative population and the rest as the positive population. Expert manual inspection and adjustment was then applied to fine tune and/or correct gate values. An example of one-dimensional GMM gating can be found in Supplementary Fig. 9. Single-cell clustering was conducted by GMM using the EMGM function in the Cyt package[70]. Briefly, each CyCIF sample's single-cell intensity data were first normalized by shifting and rescaling the 1st and 99th percentiles of each marker to 5,000 and 30,000 relative fluorescence units, respectively. Then, the inverse hyperbolic sine (asinh) function in Cyt was applied. For GMM clustering, several k values (from 6 to 15) were tested and k was chosen on the basis of concordance with visible clusters in a t-SNE visualization. The markers used in clustering were S100, MITF, AXL, CD45, vimentin, SMA, catenin and NGFR. A total of 10,000 cells from each sample were used.

Identification of tumor regions. A board-certified dermatopathologist (C.G.L.) reviewed t-CyCIF images and defined invasive margins of each sample. To heuristically define which cells belonged to intratumor regions, we first defined tumor cells as S100^{hi} cells in a two-component GMM of tumor marker (S100) intensities in each sample. Then, a k-nearest-neighbor classifier was trained on cells' xy coordinates to predict whether cells were tumor cells, for k = 25. Cells that this classifier predicted to be tumor cells were then defined to be in the intratumor regions. MATLAB code is provided in supplemental materials/methods.

Spatial enrichment analysis. Each spatial enrichment curve is defined for a tumor population (NGFR^{hi} or MITF^{hi} tumor cells from clustering) and a target population (for example immune cells). The curve represents the ratio of CDF curves for (1) pairwise distances between a chosen tumor population and a target population and (2) pairwise distances between a random tumor population and the target population. A random tumor population was defined by randomly labeling an equal number of tumor cells as the chosen tumor population. Each curve was computed by averaging results for 300 instances of random tumor populations, from a 10,000-cell subsample per tissue sample. Technically separated tissue pieces on the same slide were treated as distinct tissue samples. Differences between groups of curves were evaluated by fitting all curves in a group to an exponential and comparing fit parameters with a z-test. Fitting and confidence intervals were computed in MATLAB with fit(), using the Trust-Region algorithm with a manual initialization. Tumor population was defined as GMM clusters 3, 4, 6, 9 and 11 and the immune population was GMM cluster 1 (from Fig. 3b) for the analysis in Fig. 3d and tumor and immune populations defined by gating for the analysis in Fig. 4f.

Spatial morphology analysis of entropy and polarity. Single-cell CyCIF data were used to obtain the coordinates of particular cell types (for example NGFR$^+$). Then, density plots of cell coordinates were converted to grayscale images on which Shannon entropy was computed using the MATLAB entropy() function. To account for global distributions and shapes of individual tumors, cell-type entropy was normalized by the entropy of tumor cells (S100$^+$).

For the polarity calculation, single-cell coordinates were translated to place the centroid of all cell coordinates at the origin. Polarity of a specific cell type was defined as the net displacement of all of its cells' coordinate vectors $\vec{v}_i$, normalized by cell-type count N and scale L of each tissue sample (minimum between x or y range of coordinates):

$$\text{Polarity} = \frac{\sqrt{\left(\sum_i \vec{v_i}\right) \cdot \left(\sum_i \vec{v_i}\right)}}{NL}.$$

Immunohistochemistry. Tissue sections were deparaffinized, rehydrated and blocked with 3% hydrogen peroxide. All were stained on a Bond 3 automated immunostainer (Leica Microsystems) and Dako Autostainer (Dako Corporation) using EnVision (Dako) staining reagents. Sections were incubated for 60 min

with PTEN (BioCare Medical) or NGFR (BD Biosciences) and ERG (Abcam) and were then incubated with the EnVision+ Dual Link (Dako) detection reagent for 30 min. Sections were washed and treated with a solution of diaminobenzidine and hydrogen peroxide (Dako) for 10 min and after rinsing, a toning solution (DAB Enhancer, Dako) was used for 2 min to enrich the final color.

Single-cell RNA-seq processing and analysis. A fresh tumor sample was collected after surgery and was dissociated within half an hour using a human tumor dissociation kit (Miltenyi Biotec; 130-095-929) on a gentleMACS Octo Dissociator (Miltenyi Biotec; 130-095-937). For the neck sample, single-cell libraries were prepared with Chromium Single Cell 3′ library kits using v2 chemistry (10X Genomics) according to the manual. For the brain sample, single cells were sorted into wells on the basis of CD45 and CD3 markers or absence thereof via FACS and lysed in a buffer containing free dNTPs and oligo(dT)-tailed oligonucleotides with a universal 5′-anchor sequence and processed in accordance with the standard Smart-seq2 protocol. Transcripts from each cell were reverse transcribed in each droplet (neck) or well (brain) and barcoded cDNA was amplified in bulk. The resulting gene expression libraries were profiled by NextSeq 500 and/or NovaSeq 6000 systems (Illumina).

Sample de-multiplexing, barcode processing, alignment, filtering and unique molecular identifier counting were performed using the Cell Ranger analysis pipeline (v.3.1) for the neck sample. For the brain sample the cumulus/smartseq2/7 workflow on Terra (https://portal.fireclound.org/?return=terra#methods/cumulus/smartseq2/7) was used for preprocessing and alignment, with the GRCh38_ens93filt reference. Downstream analyses were performed in R using the Seurat[71] package (v.3.1.0) and in Python with the scanpy package (v.1.4.4.post1)[72].

For each cell, two quality control metrics were calculated: (1) the total number of genes detected and (2) the proportion of unique molecular identifiers contributed by mitochondrially encoded transcripts. Cells in which fewer than 200 genes were detected and in which mitochondrially encoded transcripts constituted >20% of the total library were excluded from downstream analysis, yielding an expression matrix of 8,669 cells by 17,697 genes for the 10X Genomics neck sample and 652 cells by 33,538 genes for the Smart-seq2 brain sample. Each gene expression measurement was normalized by total expression within the corresponding cell and multiplied by a scaling factor of 10,000. Mean and standardized variance values were calculated for each gene across all cells and a subset of 5,000 highly variable genes was selected for PCA. Following PCA, UMAP was performed on the first 30 principal components using default parameters. Unsupervised clustering using the default graph-based algorithm implemented in Seurat (resolution parameter 0.2) identified nine distinct clusters (for the neck sample) and eight clusters (for the brain sample) (Supplementary Fig 7). For classification of cell populations, differential expression analysis was performed between each cluster and all other cells using a Wilcoxon rank-sum test. Clusters of malignant cells were identified using InferCNV with PTPRC+ cells as a reference population. Dimension reduction was performed on this subset of 7,844 malignant cells using PCA and UMAP as described above. Scoring of single cells with NGFR program signatures from previous literature was performed using the VISION R package[16,73,74]. In the brain sample, 220 malignant cells were characterized. In both samples, cutoffs for NGFR^{hi} tumor cells (on the basis of NGFR program signatures) were chosen to be concordant with high NGFR single gene expression within that sample and we performed a GSEA comparing NGFR^{hi} tumor cells thus defined to NGFR^{lo} tumor cells.

For pre-ranked GSEA, differential expression analysis was performed between NGFR[hi] and NGFR^{lo} cells using a Wilcoxon rank-sum test and log[2] (fold change) was selected as a ranking metric. Pre-ranked GSEA was performed using a curated collection of gene sets consisting of sets from the Hallmark collection in the MSigDB database[75].

Reporting Summary. Further information on research design is available in the Nature Research Reporting Summary linked to this article.

Data availability

All requests for raw and analyzed data and materials will be promptly reviewed by the senior author (G.M.B.) to verify whether the request is subject to any intellectual property or confidentiality obligations. Patient-related data not included in the paper may be subject to patient confidentiality. Any data and materials that can be shared will be released via a material transfer agreement. All analyzed sequencing data are in supplementary data available at the journal website and any additional data made publicly available after publication will be found at https://github.com/davidliu-lab/Pt98. All t-CyCIF tissue images are available for online viewing: https://www.cycif.org/data/liu-lin-2019/. Raw sequencing data have been deposited into dbGAP, phs001427.v2.p1, which is publicly accessible. Matched clinical and sequencing characteristics of tumors are in Supplementary Table 1.

References

47. Van Allen, E. M. et al. Whole-exome sequencing and clinical interpretation of formalin-fixed, paraffin-embedded tumor samples to guide precision cancer medicine. *Nat. Med.* **20**, 682–688 (2014).
48. Fisher, S. et al. A scalable, fully automated process for construction of sequence-ready human exome targeted capture libraries. *Genome Biol.* **12**, R1 (2011).
49. Gnirke, A. et al. Solution hybrid selection with ultra-long oligonucleotides for massively parallel targeted sequencing. *Nat. Biotechnol.* **27**, 182–189 (2009).
50. Cibulskis, K. et al. ContEst: estimating cross-contamination of human samples in next generation sequencing data. *Bioinformatics* **27**, 2601–2602 (2011).
51. Lawrence, M. S. et al. Discovery and saturation analysis of cancer genes across 21 tumour types. *Nature* **505**, 495–501 (2014).
52. Hodis, E. et al. A landscape of driver mutations in melanoma. *Cell* **150**, 251–263 (2012).
53. Cibulskis, K. et al. Sensitive detection of somatic point mutations in impure and heterogeneous cancer samples. *Nat. Biotechnol.* **31**, 213–219 (2013).
54. Saunders, C. T. et al. Strelka: accurate somatic small-variant calling from sequenced tumor–normal sample pairs. *Bioinformatics* **28**, 1811–1817 (2012).
55. Ramos, A. H. et al. Oncotator: cancer variant annotation tool. *Hum. Mutat.* **36**, E2423–E2429 (2015).
56. Costello, M. et al. Discovery and characterization of artifactual mutations in deep coverage targeted capture sequencing data due to oxidative DNA damage during sample preparation. *Nucleic Acids Res.* **41**, e67 (2013).
57. Olshen, A. B., Venkatraman, E. S., Lucito, R. & Wigler, M. Circular binary segmentation for the analysis of array-based DNA copy number data. *Biostatistics* **5**, 557–572 (2004).
58. Shen, R., Olshen, A. B. & Ladanyi, M. Integrative clustering of multiple genomic data types using a joint latent variable model with application to breast and lung cancer subtype analysis. *Bioinformatics* **25**, 2906–2912 (2009).
59. Carter, S. L. et al. Absolute quantification of somatic DNA alterations in human cancer. *Nat. Biotechnol.* **30**, 413–421 (2012).
60. Brastianos, P. K. et al. Genomic characterization of brain metastases reveals branched evolution and potential therapeutic targets. *Cancer Discov.* **5**, 1164–1177 (2015).
61. Burrell, R. A. et al. Replication stress links structural and numerical cancer chromosomal instability. *Nature* **494**, 492–496 (2013).
62. Roth, A. et al. PyClone: statistical inference of clonal population structure in cancer. *Nat. Methods* **11**, 396–398 (2014).
63. Leshchiner, I. et al. Comprehensive analysis of tumour initiation, spatial and temporal progression under multiple lines of treatment. Preprint at *bioRxiv* https://doi.org/10.1101/508127 (2018).
64. Li, B. & Dewey, C. N. RSEM: accurate transcript quantification from RNA-seq data with or without a reference genome. *BMC Bioinf.* **12**, 323 (2011).
65. Shukla, S. A. et al. Comprehensive analysis of cancer-associated somatic mutations in class I HLA genes. *Nat. Biotechnol.* **33**, 1152 (2015).
66. Jurtz, V. et al. NetMHCpan-4.0: improved peptide-MHC class I interaction predictions integrating eluted ligand and peptide binding affinity data. *J. Immunol.* **199**, 3360–3368 (2017).
67. Hundal, J. et al. pVAC-seq: a genome-guided in silico approach to identifying tumor neoantigens. *Genome Med.* **8**, 11 (2016).
68. Lin, J.-R. et al. Highly multiplexed immunofluorescence imaging of human tissues and tumors using t-CyCIF and conventional optical microscopes. *eLife* https://doi.org/10.7554/eLife.31657 (2018).
69. Lin, J.-R., Fallahi-Sichani, M. & Sorger, P. K. Highly multiplexed imaging of single cells using a high-throughput cyclic immunofluorescence method. *Nat. Commun.* **6**, 8390 (2015).
70. Amir, E. D. et al. viSNE enables visualization of high dimensional single-cell data and reveals phenotypic heterogeneity of leukemia. *Nat. Biotechnol.* **31**, 545–552 (2013).
71. Satija, R., Farrell, J. A., Gennert, D., Schier, A. F. & Regev, A. Spatial reconstruction of single-cell gene expression data. *Nat. Biotechnol.* **33**, 495–502 (2015).
72. Wolf, F. A., Angerer, P. & Theis, F. J. SCANPY: large-scale single-cell gene expression data analysis. *Genome Biol.* **19**, 15 (2018).
73. DeTomaso, D. et al. Functional interpretation of single cell similarity maps. *Nat. Commun.* **10**, 4376 (2019).
74. Tirosh, I. et al. Dissecting the multicellular ecosystem of metastatic melanoma by single-cell RNA-seq. *Science* **352**, 189–196 (2016).
75. Subramanian, A. et al. Gene set enrichment analysis: a knowledge-based approach for interpreting genome-wide expression profiles. *Proc. Natl Acad. Sci. USA* **102**, 15545–15550 (2005).

Author contributions

Competing interests

Additional information

Extended data is available for this paper at https://doi.org/10.1038/s41591-021-01331-8.

Supplementary information The online version contains supplementary material available at https://doi.org/10.1038/s41591-021-01331-8.

Correspondence and requests for materials should be addressed to G.M.B.

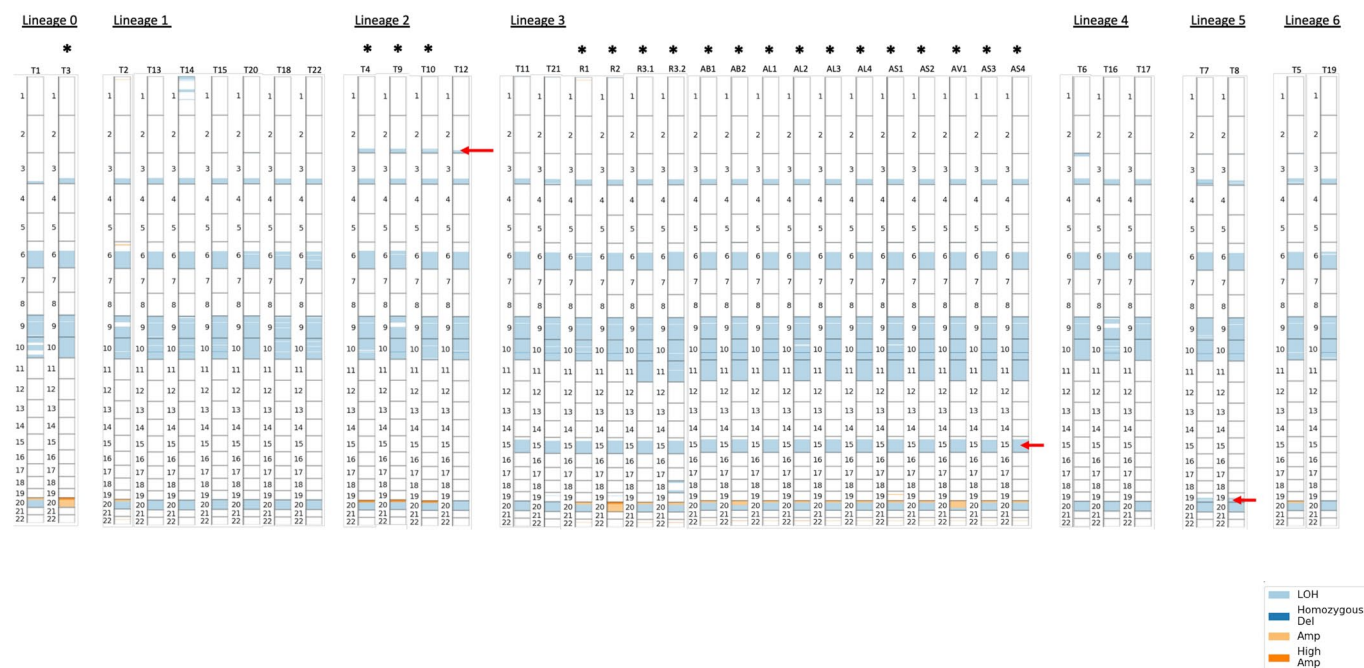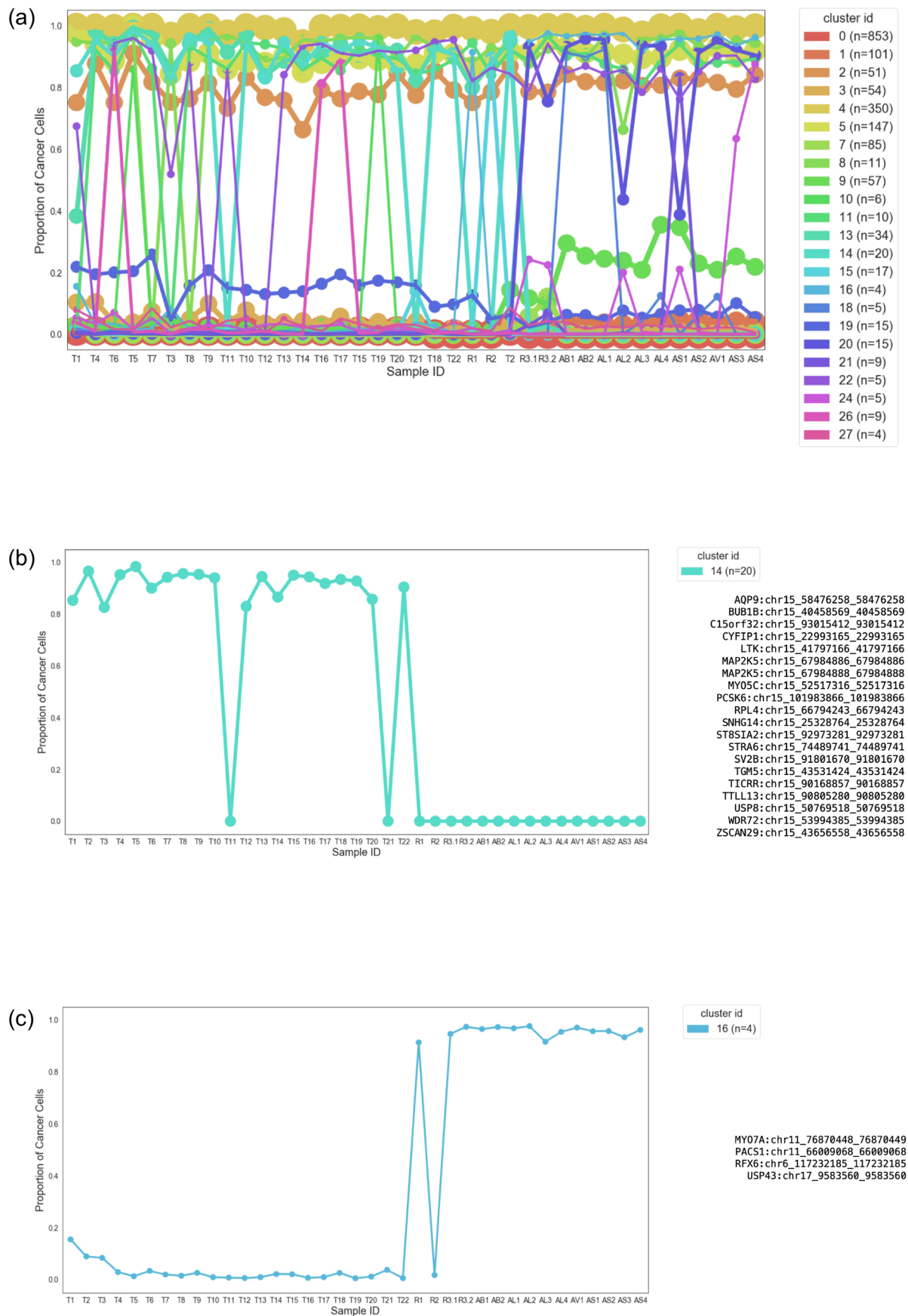**Reprints and permissions information** is available at www.nature.com/reprints.

Extended Data Fig. 1 | Mutation Load and Mutations in Significant Melanoma Genes. 221 nonsynonymous clonal mutations were found in all tumors, including hotspot mutations in IDH1 (p.R132C) and MAP2K1 (p.E203K), and additional missense mutations in cancer driver genes CTNNB1 (p.R582W) and ARID2 (p.P1664S).

Extended Data Fig. 2 | Mutational Spectrum Profile of Common Ancestor. 489 common single nucleotide variants (including non-coding mutations) found in all tumors with mutations called individually in each sample are represented in their tri-nucleotide context; this mutational spectrum has cosine similarity of 0.965 with the ultraviolet DNA damage signature (Signature 7; https://cancer.sanger.ac.uk/cosmic/signatures). A similar analysis with 548 common ancestor mutations inferred jointly by PyClone generates similar results with cosine similarity of 0.962 to the UV signature (not shown).

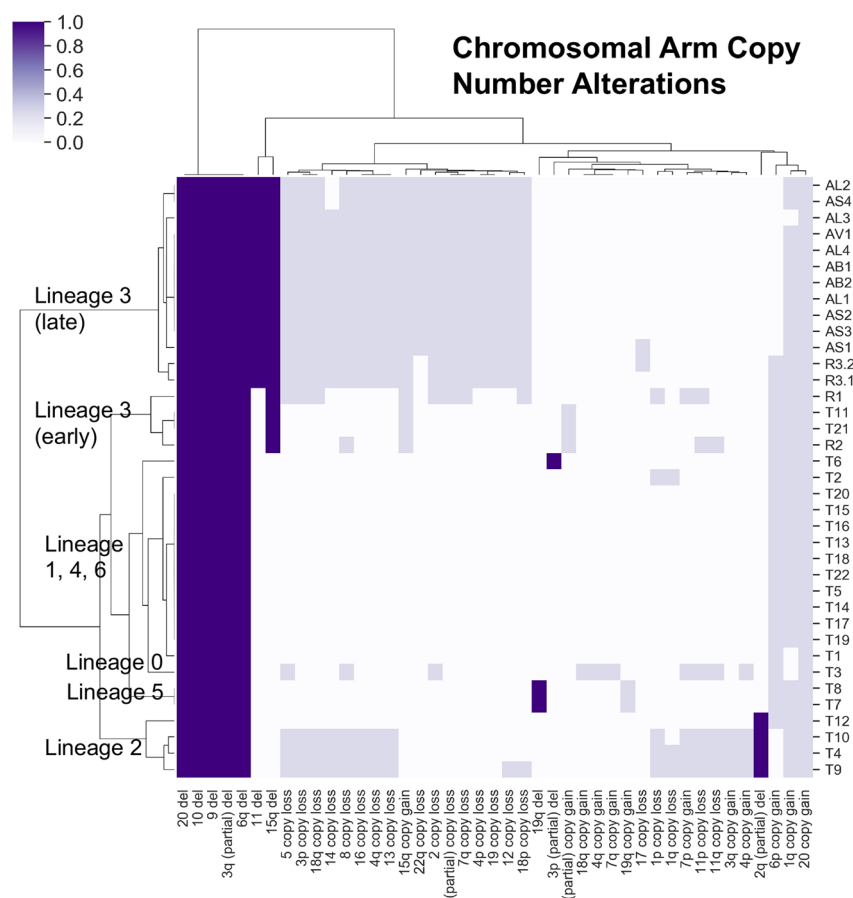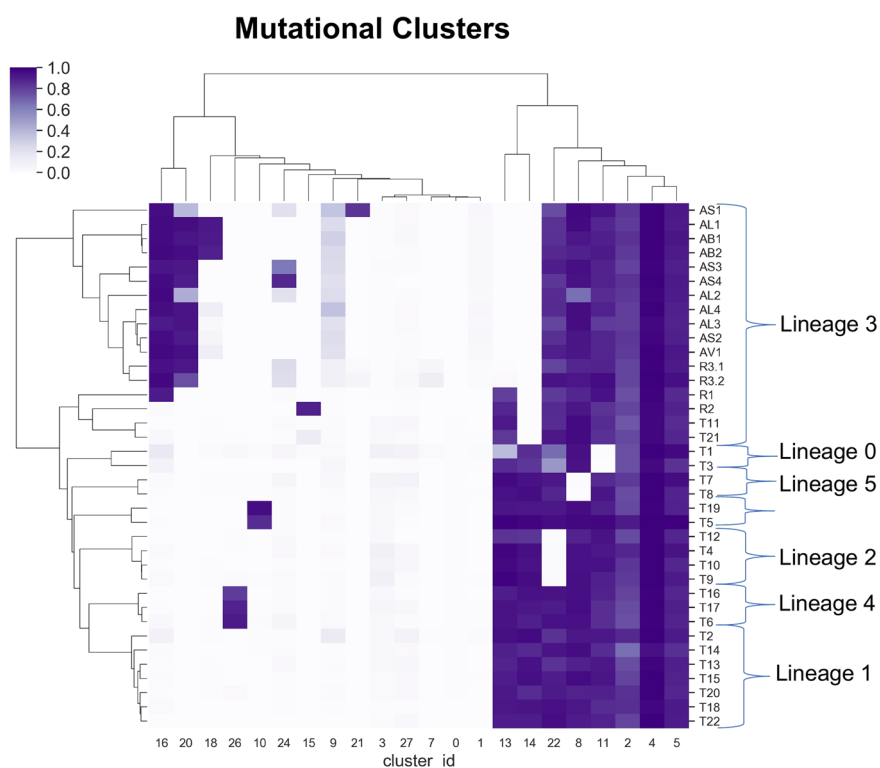**Extended Data Fig. 3 | Copy Number Alterations by Lineage and Tumor.** Each bar represents a tumor, with numbers indicating chromosomes and copy number alterations indicated by shade. Red arrows indicate the chromosomal segment loss of heterozygosity with corresponding loss of mutations in that segment that characterize the lineage, that is 2q for Lineage 2, 15q in Lineage 3, 19q in Lineage 5. Genome doubling is indicated by *.

(a)

(b)

AQP9:chr15_58476258_58476258
BUB1B:chr15_40458569_40458569
C15orf32:chr15_93015412_93015412
CYFIP1:chr15_22993165_22993165
LTK:chr15_41797166_41797166
MAP2K5:chr15_67984886_67984886
MAP2K5:chr15_67984888_67984888
MYO5C:chr15_52517316_52517316
PCSK6:chr15_101983866_101983866
RPL4:chr15_66794243_66794243
SNHG14:chr15_25328764_25328764
ST8SIA2:chr15_92973281_92973281
STRA6:chr15_74489741_74489741
SV2B:chr15_91801670_91801670
TGM5:chr15_43531424_43531424
TICRR:chr15_90168857_90168857
TTLL13:chr15_90805280_90805280
USP8:chr15_50769518_50769518
WDR72:chr15_53994385_53994385
ZSCAN29:chr15_43656558_43656558

(c)

MYO7A:chr11_76870448_76870449
PACS1:chr11_66009068_66009068
RFX6:chr6_117232185_117232185
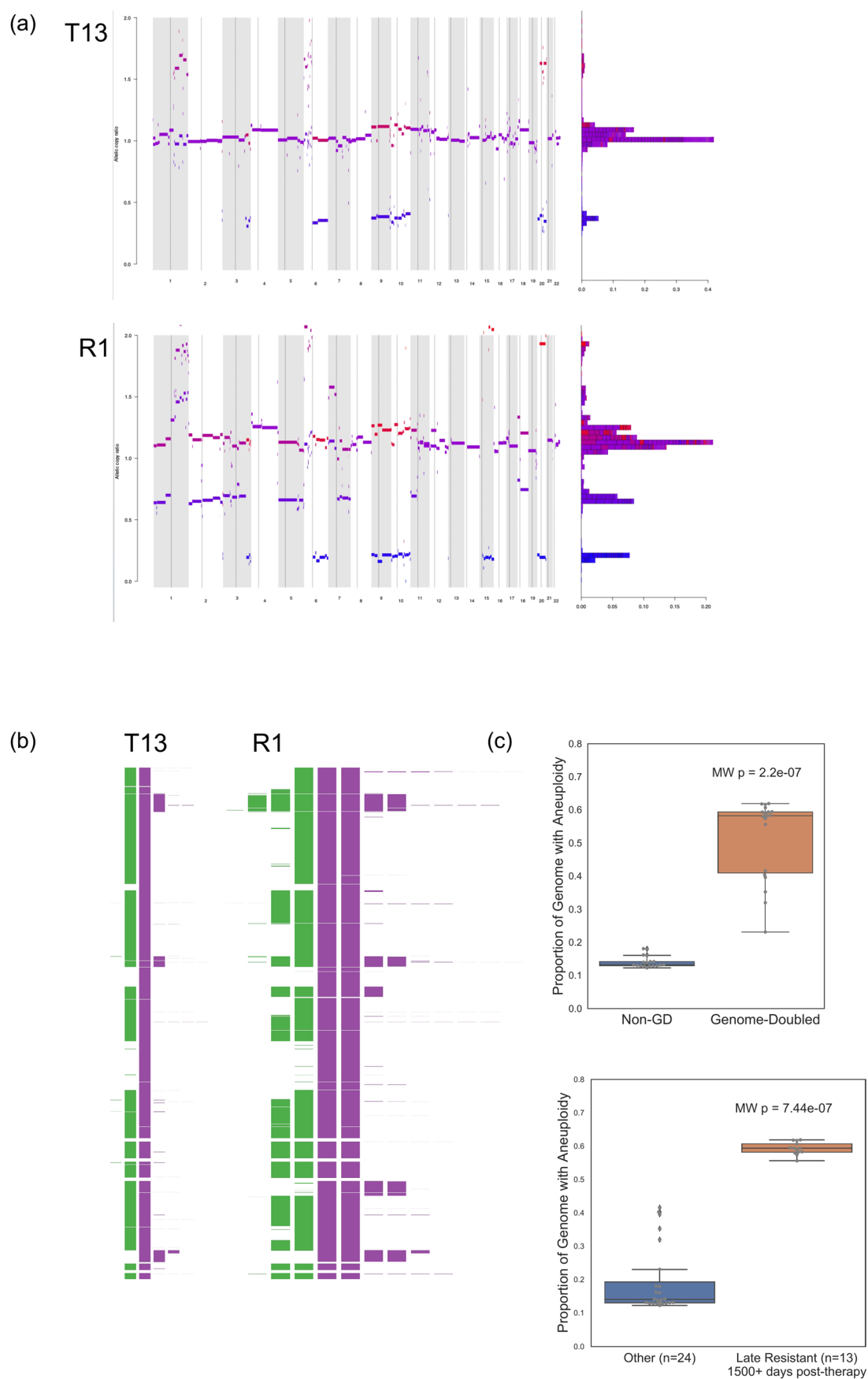USP43:chr17_9583560_9583560

Extended Data Fig. 4 | See next page for caption.

Extended Data Fig. 4 | Inferred Lineage-Defining Mutational Clusters and Cancer Cell Fractions by Tumor. a, Inferred Mutational Clusters and Cluster Cancer Cell Fraction by Tumor. Mutational clusters representing subclones and the proportion of cancer cells in each tumor sample with each mutational cluster was inferred using PyClone. The x-axis shows each tumor, the y-axis is the proportion of cancer cells in each sample containing the cluster, and the legend (n=xx) refers to the number of mutations for each inferred cluster. Only clusters containing more than 3 mutations were included (9 clusters excluded) in subsequent analyses. **b**, Mutational Cluster Defining Lineage 3. This pattern demonstrates the loss of mutations in a common ancestor of the seventeen tumors in Lineage 3 (T11, T21, the early escape lesions (R1 and R2) and late-emerging resistant lesions (R2 and R3.2) and the post-autopsy lesions). These mutations are all found in chromosome 15, with a corresponding LOH in chromosome 15q. **c**, Mutational Cluster Defining Early Resistant Small Bowel Metastasis. This cluster represents the acquired mutations shared between the small bowel metastasis (R1) and the other late resistant tumors which also share a bi-allelic *CDKN2A* deletion. 2/4 mutations were inferred to have multiplicity of 2, and 2/4 multiplicity of 1, consistent with a unique genome doubling event just prior to the emergence of this tumor in lineage 3, and present in all subsequent resistant tumors. These mutations were manually reviewed and showed no evidence of artifact, although *MYO7A* is detectable at a lower level in P4 than the subsequent resistant tumors.
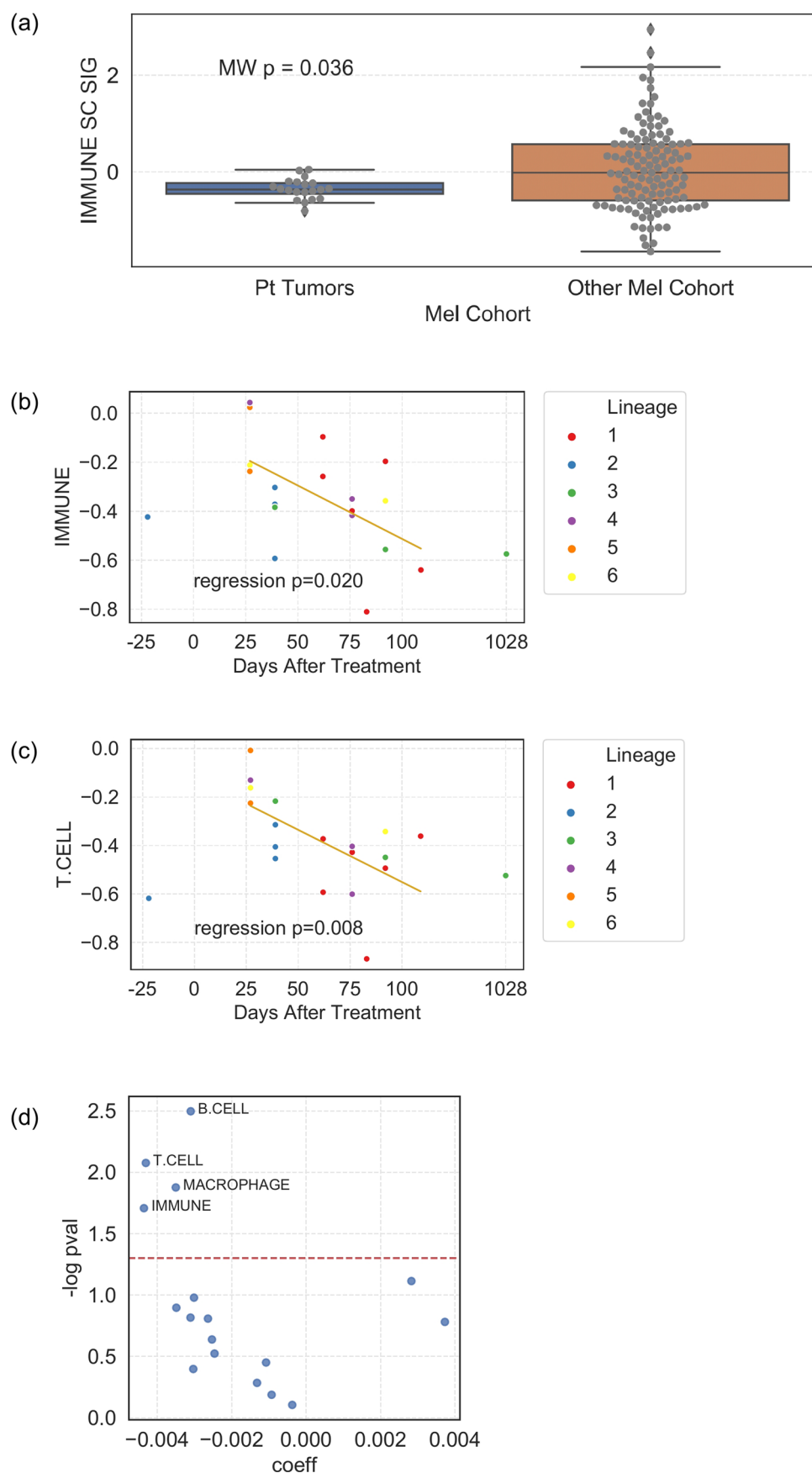
Extended Data Fig. 5 | See next page for caption.

Extended Data Fig. 5 | Hierarchical Clustering of Mutational Clusters CCFs and Copy Number Alterations define concordant tumor lineages. Top: Hierarchically clustered heatmap of inferred cancer cell fractions (CCFs) for each mutation cluster (columns) for each tumor (rows), demonstrating 7 different lineages. Bottom: Hierarchically clustered heatmap of large copy number alterations (columns) for each tumor (rows), demonstrating concordance with lineages derived from mutational clusters. Complete allelic deletions are dark blue, and copy number gains and losses are light blue.
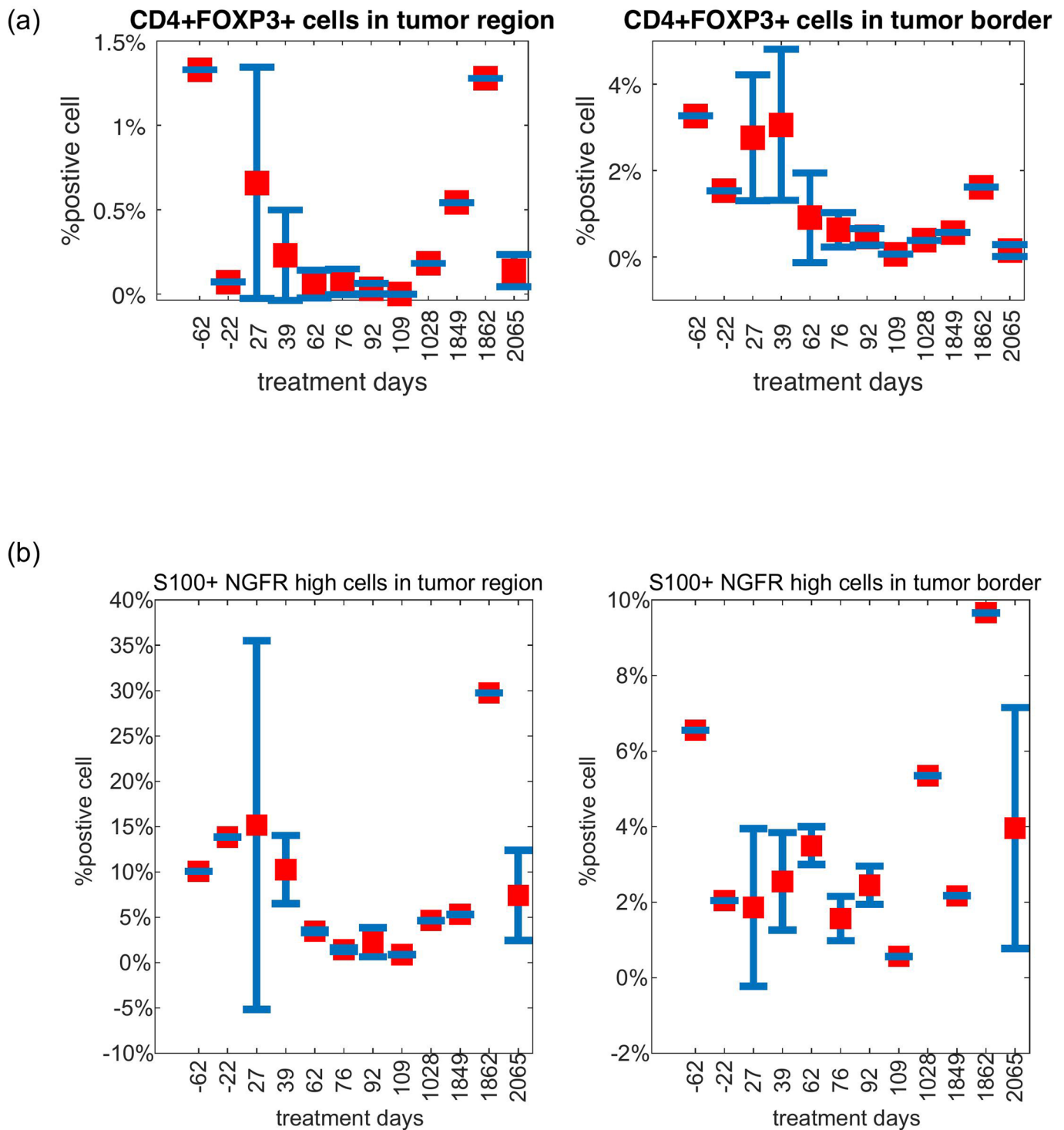
Extended Data Fig. 5 | Hierarchical Clustering of Mutational Clusters CCFs and Copy Number Alterations define concordant tumor lineages.

(a) T13

(a) R1

(b) T13   R1   (c)

Extended Data Fig. 6 | See next page for caption.

Extended Data Fig. 6 | Aneuploidy in Genome-Doubled vs. non-Genome-Doubled tumors. Aneuploidy here is defined as the proportion of the genome with copy number gain or loss (compared to the 'baseline' allelic copy number, which is 1 for non-genome doubled tumors and 2 for genome doubled tumors). **a**, Allelic copy number ratios for a representative non-genome doubled tumor (T13 from lineage 1, upper), and a genome-doubled tumor (R1, the jejunal metastasis from lineage 3, lower). The x axis is the genome (chromosomes in increasing number), and y represents the relative inferred copy number at that genomic location. **b**, A different representation of the inferred allelic copy from T13 and R1 demonstrating increased aneuploidy in the genome-doubled tumor. **c**, The genome doubled tumors (n=19) had evidence of chromosomal instability, with higher proportion of genome with aneuploidy (two-sided Mann-Whitney p=2.2e-07, Methods) compared to non-genome doubled tumors (n=18) (upper panel). Late resistant tumors (D1500+) had the higher aneuploidy compared to all other tumors, (lower panel). Boxplots: box limits indicate the IQR (25th to 75th percentiles), with a center line indicating the median. Whiskers show the value ranges up to 1.5×IQR above the 75th or below the 25th percentiles, with outliers beyond those ranges shown as individual points.
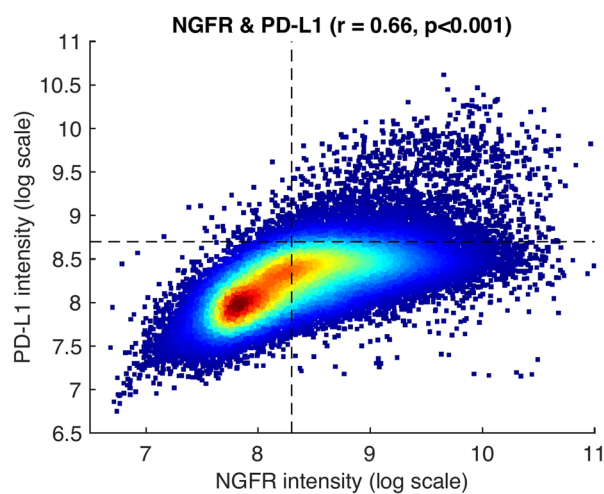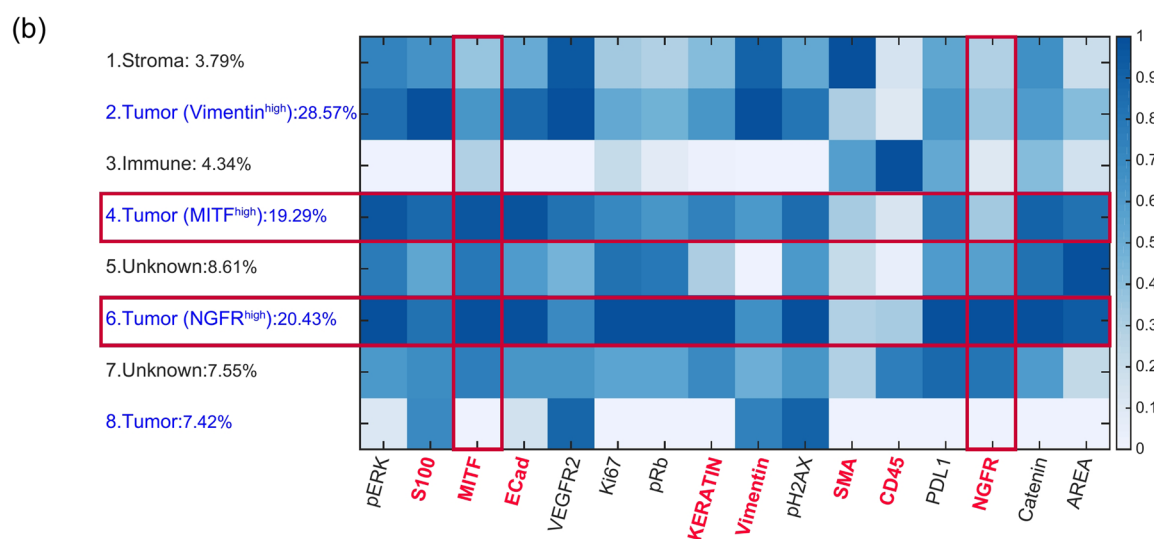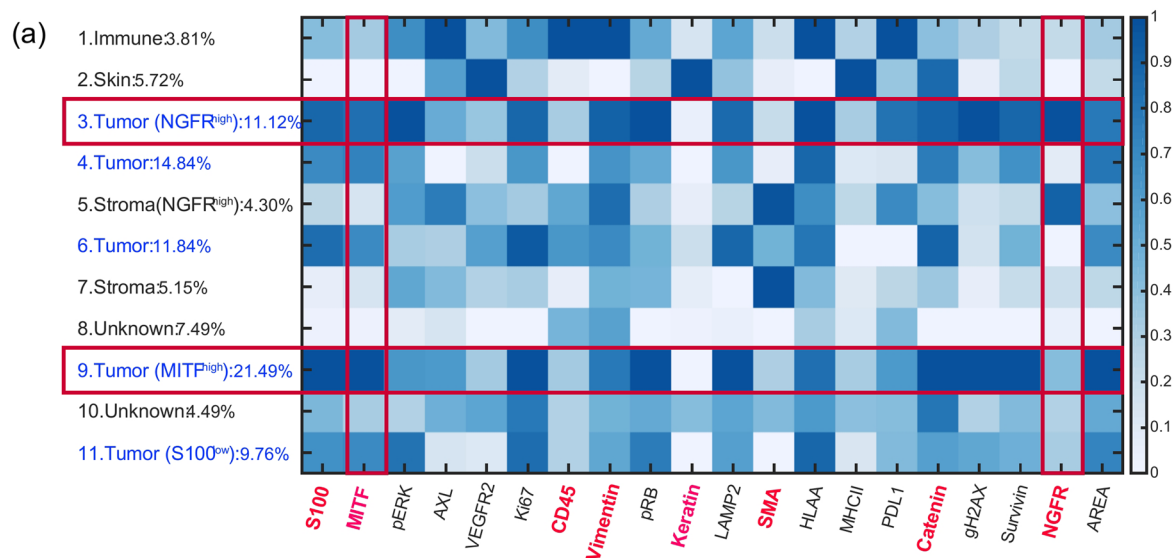
Extended Data Fig. 7 | See next page for caption.

Extended Data Fig. 7 | Tumor Immune Microenvironment. a, Tumors from the patient (n=20) had lower overall immune signature score compared to a large cohort of PD-1 treated melanoma patients (n=121) (MWW nominal two-sided p = 0.036);. **b**, overall Immune signature scores in tumors biopsied within the first 120 days after immunotherapy initiation decreased after initiation of immune checkpoint blockade (linear regression p = 0.020). **c**, T cell signature scores in the same tumors decrease after initiation of immune checkpoint blockade (linear regression p = 0.008). **d**, All immune cell signature scores in the same tumors and their association with time after treatment. Negative coefficients are associated with a decrease in score with time after treatment. Boxplots: box limits indicate the IQR (25th to 75th percentiles), with a center line indicating the median. Whiskers show the value ranges up to 1.5 × IQR above the 75th or below the 25th percentiles, with outliers beyond those ranges shown as individual points.

(a)

(b)

Extended Data Fig. 8 | Quantification of Selected Immune and Tumor Populations from CyCIF. Selected immune cell and NGFR-high subset proportions **over time by spatial compartment**. (**a**) CD4 + Treg cells; (**b**) NGFR-high tumor cells. Error bars represent standard error of the mean (S.E.M.). Sample numbers for each days are: 1(day -62), 1(day -22), 4(day 4), 4(day 39), 2(day 62), 3(day 76), 3(day 92), 1(day 109), 1(day 1028), 1(day 1849), 1(day 1862), 10(day 2065).

Extended Data Fig. 9 | See next page for caption.

Extended Data Fig. 9 | Gaussian Mixture Modelling of CyCIF data. a, Heatmap demonstrating clusters of cells from Gaussian Mixture Model clustering characterized by a range of CyCIF quantitative fluorescence (Methods) from the 19 tumors in Batch 1. **b**, Heatmap demonstrating clusters of cells from Gaussian Mixture Model clustering characterized by a range of CyCIF quantitative fluorescence (Methods) from the pre- and post-TLR9 + antiPD1 therapy tumors (Batch 2). (Top) There is a distinct NGFR-Hi tumor cell cluster, which is high in PD-L1 protein expression, a MITF-Hi/NGFR-lo tumor cell cluster, and an immune cell cluster. Several non-specific (that is non-NGFR-Hi, non-MITF-Hi) tumor cell clusters are also seen. (Bottom) There is a strong association between NGFR and PD-L1 expression among S100 + gated tumor cells (Pearson correlation coefficient r = 0.66 and p-value = 0, calculated by the default function in MATLAB).

Extended Data Fig. 10 | See next page for caption.

Extended Data Fig. 10 | Expression of class I and class II MHC and of clonal ancestral neoantigens in lineage 3 and over time. a, MHC-I and –II scores were generated from bulk RNAseq and compared between Lineage 3 tumors (n=3) and other tumors (n=17). Scores for each sample were calculated using an averaged standardized z-score of 6 MHC-I genes (*HLA-A, HLA-B, HLA-C, B2M, TAP1, TAP2*) and 13 MHC-II genes (*HLA-DMA, HLA-DMB, HLA-DOA, HLA-DOB, HLA-DPA1, HLA-DPB1, HLA-DQA1, HLA-DQA2, HLA-DQB1, HLA-DQB2, HLA-DRA, HLA-DRB1, HLA-DRB5*). (Left) Lineage 3 has lower MHC-I score compared to other tumors (t-test p = 0.01). (Right) Lineage 3 tumors do not have a statistically significant difference in MHC-II score compared to other tumors (t-test p = 0.13). **b**, Expression of clonal ancestral neoantigens in lineage 3 and over time. Neoantigens were inferred using NetMHCPan with inputs of the patient's HLA and mutations. 174 genes with clonal ancestral mutations that coded for neoantigens were identified, and their RNAseq expression (TPM) in each tumor calculated. Overall expression, Chr15 neoantigen expression (that is the expression of the 3 genes with clonal ancestral mutations lost with LOH of Chr15 in Lineage 3 tumors), and the proportion of the overall neoantigen expression that Chr15 neoantigen genes represented were calculated. Left: Lineage 3 vs other tumors. Overall expression was not different, but there was a trend towards lower expression and proportion of expression of Chr15 neoantigen genes in Lineage 3 tumors. Right: Expression over time in the on-treatment time period (D27-D109). Overall neoantigen gene expression was not different by time, but Chr15 neoantigen gene expression and the proportion of Chr15 neoantigen gene expression trended towards decreasing with time. Boxplots: box limits indicate the IQR (25th to 75th percentiles), with a center line indicating the median. Whiskers show the value ranges up to 1.5 × IQR above the 75th or below the 25th percentiles, with outliers beyond those ranges shown as individual points.

nature research

Corresponding author(s): Genevieve Boland

Last updated by author(s): Mar 8, 2021

Reporting Summary

Nature Research wishes to improve the reproducibility of the work that we publish. This form provides structure for consistency and transparency in reporting. For further information on Nature Research policies, see Authors & Referees and the Editorial Policy Checklist.

Statistics

For all statistical analyses, confirm that the following items are present in the figure legend, table legend, main text, or Methods section.

n/a	Confirmed	
☐	☒	The exact sample size (*n*) for each experimental group/condition, given as a discrete number and unit of measurement
☐	☒	A statement on whether measurements were taken from distinct samples or whether the same sample was measured repeatedly
☐	☒	The statistical test(s) used AND whether they are one- or two-sided *Only common tests should be described solely by name; describe more complex techniques in the Methods section.*
☐	☒	A description of all covariates tested
☐	☒	A description of any assumptions or corrections, such as tests of normality and adjustment for multiple comparisons
☐	☒	A full description of the statistical parameters including central tendency (e.g. means) or other basic estimates (e.g. regression coefficient) AND variation (e.g. standard deviation) or associated estimates of uncertainty (e.g. confidence intervals)
☐	☒	For null hypothesis testing, the test statistic (e.g. *F*, *t*, *r*) with confidence intervals, effect sizes, degrees of freedom and *P* value noted *Give P values as exact values whenever suitable.*
☒	☐	For Bayesian analysis, information on the choice of priors and Markov chain Monte Carlo settings
☒	☐	For hierarchical and complex designs, identification of the appropriate level for tests and full reporting of outcomes
☒	☐	Estimates of effect sizes (e.g. Cohen's *d*, Pearson's *r*), indicating how they were calculated

Our web collection on statistics for biologists contains articles on many of the points above.

Software and code

Policy information about availability of computer code

Data collection	No software was used for data collection.
Data analysis	All analytical techniques are described and cited in the Methods section. Results generated using publically available websites/tools with parameters are described in Methods.
	WES Pipeline available at https://portal.firecloud.org/#methods/getzlab/CGA_WES_Characterization_Pipeline_v0.1_Dec2018/ including:
	Mutect (v1.1.6); Strelka (v.1.0.11); PyClone(v0.13.1); GATK4 (v4.0.5.1), ABSOLUTE (v1.5);
	Other software packages:
	STAR(v2.4.1a);RSEM(v1.2.15); NetMHCPan (v4.0), pVAC-seq (v4.0); Seurat (v3.1.0); VISION (1.1.0);
	PHYLOGICNDT (https://github.com/broadinstitute/PhylogicNDT, no version available), ONCOTATOR (v2.7.1);
	Python packages: seaborn(v0.9.0); scipy(v1.1.0); statsmodels(0.9.0); scanpy (v1.4.4.post1)
	Websites:
	GSEA(https://cloud.genepattern.org)
	CIBERSORT (http://cibersort.stanford.edu)

For manuscripts utilizing custom algorithms or software that are central to the research but not yet described in published literature, software must be made available to editors/reviewers. We strongly encourage code deposition in a community repository (e.g. GitHub). See the Nature Research guidelines for submitting code & software for further information.

Data

Policy information about <u>availability of data</u>

All manuscripts must include a <u>data availability statement</u>. This statement should provide the following information, where applicable:
- Accession codes, unique identifiers, or web links for publicly available datasets
- A list of figures that have associated raw data
- A description of any restrictions on data availability

All requests for raw and analyzed data and materials will be promptly reviewed by the senior author (Dr. Boland) to verify if the request is subject to any intellectual property or confidentiality obligations. Patient-related data not included in the paper may be subject to patient confidentiality. Any data and materials that can be shared will be released via a Material Transfer Agreement. All analyzed sequencing data are in supplementary data available at the journal website, and any additional data made publicly available after publication will be found at https://github.com/davidliu-lab/Pt98. All t-CyCIF tissue images are available for online viewing: https://www.cycif.org/data/liu-lin-2019/. Raw sequencing data have been deposited into dbGAP, phs001427.v2.p1, which is publicly accessible. Matched clinical and sequencing characteristics of tumors are in Supplementary Table 1.

Field-specific reporting

Please select the one below that is the best fit for your research. If you are not sure, read the appropriate sections before making your selection.

☒ Life sciences   ☐ Behavioural & social sciences   ☐ Ecological, evolutionary & environmental sciences

For a reference copy of the document with all sections, see nature.com/documents/nr-reporting-summary-flat.pdf

Life sciences study design

All studies must disclose on these points even when the disclosure is negative.

Sample size	n = 37 tumors from 1 patient. No necessary sample size was determined as these were available tumors from this patient.
Data exclusions	Tumors were excluded on pre-established quality-control metrics: mean target coverage (> 50x), contamination estimation (< 5%), tumor purity (<10% and no matched mutations in significantly mutated genes), with a total of 3 tumors excluded for low tumor purity (37 final tumor samples).
Replication	This is a longitudinal descriptive study so no replication was possible.
Randomization	This was not an experiment, and there was no randomization for this longitudinal descriptive study within one patient.
Blinding	There were no group allocations and no blinding on this retrospective observational study of a single patient.

Reporting for specific materials, systems and methods

We require information from authors about some types of materials, experimental systems and methods used in many studies. Here, indicate whether each material, system or method listed is relevant to your study. If you are not sure if a list item applies to your research, read the appropriate section before selecting a response.

Materials & experimental systems

n/a	Involved in the study
☐	☒ Antibodies
☒	☐ Eukaryotic cell lines
☒	☐ Palaeontology
☒	☐ Animals and other organisms
☐	☒ Human research participants
☐	☒ Clinical data

Methods

n/a	Involved in the study
☒	☐ ChIP-seq
☒	☐ Flow cytometry
☒	☐ MRI-based neuroimaging

Antibodies

Antibodies used	See attached antibody table (Supplementary Table 3) with vendor identifier and links.
Validation	Most of these antibodies were validated in previous publications: Ref1: https://elifesciences.org/articles/31657 Ref2: https://www.nature.com/articles/s41596-019-0206-y

Ref3: https://www.sciencedirect.com/science/article/pii/S0092867418311784

All these antibodies are commercially available and validated by vendors as information in their websites, which links are provided in supplementary table 3. In additional, all antibodies used were re-validated in-house using the protocols described in Ref1 & Ref2, with information and images provided at:

https://www.cycif.org/antibodies

One additional antibody was newly used in this study (anti-NGFR, BD Cat. 560326). We followed the protocol described above as well as cross-referring with the previously validated NGFR antibody (anti-NGFR, abcam Cat. Ab195180).

All these antibodies are commercially available and these vendors provide validations/publications in their websites. All of them could be found on our website www.cycif.org, and links are provided in the attached antibody table.

Human research participants

Policy information about studies involving human research participants

Population characteristics	A single 67-yr old man was identified with extraordinary clinical response to immune checkpoint blockade with multiple tumor samples available for molecular characterization.
Recruitment	The patient's unusual clinical course (abrupt clinical response after disease progression on immune checkpoint blockade) was noted by his clinicians, as well as the unusual number of longitudinal tumor samples clinically biopsied. This is a longitudinal case study which may not be representative of all melanoma patients, which we discussed in the manuscript. After discussion of the potential benefits and risks, the patient gave informed consent to make his tumor samples available for molecular characterization and research.
Ethics oversight	IRB approval was obtained from the Dana-Farber/HarvardCancerCare IRB (Protocol 11-181)

Note that full information on the approval of the study protocol must also be provided in the manuscript.

Clinical data

Policy information about clinical studies

All manuscripts should comply with the ICMJE guidelines for publication of clinical research and a completed CONSORT checklist must be included with all submissions.

Clinical trial registration	This is not a clinical trial.
Study protocol	DF/HCC Protocol 11-181.
Data collection	Clinical data was abstracted from chart review over the course of the patient's treatments.
Outcomes	Response to therapy was defined using modified RECIST 1.1 criteria.